Available online at www.sciencedirect.com
SCIENCE DIRECT®
Journal of Computational Physics 193 (2004) 469–510
JOURNAL OF COMPUTATIONAL PHYSICS
www.elsevier.com/locate/jcp

A particle-level set-based sharp interface cartesian grid method for impact, penetration, and void collapse

L.B. Tran *, H.S. Udaykumar

Department of Mechanical and Industrial Engineering, The University of Iowa, Iowa City, IA 52242, USA

Received 25 April 2003; received in revised form 15 July 2003; accepted 16 July 2003

Abstract

An Eulerian, sharp interface, Cartesian grid method is developed for the numerical simulation of the response of materials to impact, shocks and detonations. The mass, momentum, and energy equations are solved along with evolution equations for deviatoric stresses and equivalent plastic strain. These equations are cast in Eulerian conservation law form. The Mie–Grüneisen equation of state is used to obtain pressure and the material is modeled as a Johnson–Cook solid. The ENO scheme is employed to capture shocks in combination with a hybrid particle level set technique to evolve sharp immersed boundaries. The numerical technique is able to handle collisions between multiple materials and can accurately compute the dynamics of the immersed boundaries. Results of calculations for axisymmetric Taylor bar impact and penetration of a Tungsten rod into steel plate show good agreement with moving finite element solutions and experimental results. Qualitative agreement with theory is shown for the void collapse phenomenon in an impacted material containing a spherical void.
© 2003 Elsevier B.V. All rights reserved.

1. Introduction

An Eulerian methodology is presented for computing a range of problems that can be classified as *high-speed multimaterial interactions* [1,2]. Such interactions can arise in phenomena such as munition–target interactions, geological impact dynamics, shock-processing of powders, formation of shaped charges upon detonation and their subsequent interaction with targets, and the impact-induced detonation of porous high-explosives.

The fundamental challenges to a simulation capability designed to solve problems in the physical phenomena listed above arise from the presence of nonlinear wave propagation and the large deformations suffered by the interacting materials. Therefore, to simulate the physics of multimaterial interactions, the numerical approach should be able to track the propagating boundaries and shock waves simultaneously and accurately. Traditionally, methods that have been used to solve such problems have been termed

* Corresponding author.
E-mail addresses: ltran@engineering.uiowa.edu (L.B. Tran), ush@engineering.uiowa.edu (H.S. Udaykumar).

0021-9991/$ - see front matter © 2003 Elsevier B.V. All rights reserved.
doi:10.1016/j.jcp.2003.07.023

hydrocodes. The broad range of available hydrocodes has been reviewed by Anderson [3] and Benson [4]. The wide variety of available methods indicates that both computational research in this area has been a robust enterprise and the existing methods all carry limitations that have spurred continuing development efforts.

Hydrocodes treat the moving material boundaries by either allowing the boundaries to flow through a fixed mesh while computing the flow field on the fixed mesh, or by allowing the mesh to follow the material points in the deforming materials. An intermediate approach, ALE (arbitrary Lagrangian–Eulerian), allows the mesh to move so as to conform to the contours of the deforming object, but the mesh is not necessarily attached to the material points. Lagrangian and arbitrary Lagrangian Eulerian (ALE) methods [5] for the simulation of problems with severe material deformation have been applied extensively in the solid mechanics community. For example, Camacho and Ortiz [6,7] have performed Lagrangian finite element calculations for impact and deformation of brittle materials [6] and ductile penetration [7]. Their approach is based on adaptive meshing, explicit contact/friction algorithm, and rate-dependent plasticity. In moving mesh methods, considerable complexity is enjoined by the need for mesh management, i.e., in maintaining an adequately refined mesh with good mesh quality. For very severe deformations, meshless methods [8–11], or a combination of finite element methods with embedded boundary tracking and local enrichment [12–14], have emerged as attractive alternatives in recent years. In these methods, one either entirely dispenses with a mesh or the mesh does not distort as the embedded boundary (such as a crack) propagates through the mesh.

Eulerian methods have been applied to study material deformation by some researchers by adapting techniques from computational fluid dynamics. For example, Trangenstein [15–17] and Trangenstein and Pember [18] have adopted Godunov's method to handle multimaterial impact as a Riemann-type problem with second-order accuracy. Benson and coworkers [19,20] have applied Eulerian methods to study the collapse of voids and shock-induced compaction in materials under impact loading. The methods presented by Benson and co-workers, although based on an Eulerian fixed mesh setting are of the Lagrangian-plus-remap type, where the material deformation calculations are split into two steps. First the material is evolved by a Lagrangian step which deforms nodes to new positions and then the field is mapped back to the fixed Eulerian mesh and the new interfaces reconstructed using Young's reconstruction. This approach has been used to good effect in the solution of mesoscale response of energetic materials in shock compression [21] and void collapse [20].

Shock-capturing methods that were developed for gas dynamics have been extended to condensed media for application to high velocity (in liquids) or high strain rate (in solids) problems where nonlinear wave propagation phenomena are important. Glaister [22] and Arienti et al. [23] employ the Roe scheme in an approximate Riemann solver to capture shocks. While the former work is restricted to gases and one dimension with a general convex equation of state, the latter deals with solid materials with the Mie–Grüneisen equation of state for the pressure, but they solve the Euler equations for the flow of the condensed material, i.e., the strength of the material is not considered. Arienti et al. [23] have also investigated two-dimensional problems in that setting. Following Dukowicz [24], Miller and Puckett [25] presented an approximate Riemann solver for multimaterials for general equations of state where material interfaces can lie within cells. They treated the multiple materials as a mixture within each cell (i.e., volume fractions) without resorting to the Lagrangian-plus-remap approach. Material strength was not considered. The discrete Riemann solver for their formulation was fairly challenging to develop, particularly at the faces of the mixed cells. A simpler approach is the Ghost Fluid Method due to Fedkiw et al. [26]. In this method the interface is treated as a sharp entity that resides on the fixed mesh and appropriate boundary conditions at the interface are applied by extrapolating the field to an extended "ghost" material. This approach leads to a local reduction in order of accuracy at the computational points adjoining the immersed interfaces. However, since such points are few in number, the overall accuracy is still maintained at the high order. Fedkiw et al. [26] have applied the ENO schemes to study

the propagation of shocks in media where the pressure is governed by a variety of equation of states (gases and liquids). Their results show that the ENO scheme can accurately handle the shock formation in such systems.

In a recently published paper [27], we presented an Eulerian methodology to simulate high-speed impact of materials. The ENO scheme was used along with explicit interface tracking and a Prandtl–Reuss material model to describe elasto-plastic deformation. Validation exercises were carried out for one-dimensional hydrodynamic and elasto-plastic impact situations. These one-dimensional results showed good agreement with exact solutions and with a Lagrangian technique using a moving mesh. Although a third-order ENO scheme was used the fact that the material was only weakly compressible rendered the captured discontinuities to be somewhat more smeared than for strong hydrodynamic shocks. Sharpening of the shock by use of different limiters along with the ENO scheme was studied. Based on this study, the Local-Lax Friedrichs ENO scheme with the minmod limiter was found to be the most robust and captured the physical features of elasto-plastic waves with optimal resolution. The present paper advances the methodology by employing the hybrid particle level set method to track boundaries and by incorporating rate-dependent plasticity (through the Johnson–Cook model) to better represent the dynamics. In addition, substantial improvements and simplifications in application of interface conditions are derived from the level-set representation.

The characteristics of the present numerical method that make it attractive relative to other methods employed in hydrocodes (including our previous work presented in [27]) for high-speed multimaterial flows are:

1. The equations governing the material deformation are solved in an Eulerian setting on a fixed Cartesian mesh. Well-developed high-accuracy shock capturing schemes are easily applied to compute the nonlinear wave-propagation phenomena in this framework. Here, the ENO scheme is used for all calculations. Addition of problem-dependent shock viscosity is not called for since adequate dissipation at discontinuities is built into the scheme.
2. The mesh remains fixed while the material flows through the mesh. Thus, issues such as mesh deformation, entangling, catastrophic mesh distortion in regions that have changed phase from solid to liquid and thus have lost strength, do not arise within the current fixed-grid approach. The materials can fragment or collide and/or merge without affecting the flow calculations.
3. The interfaces are tracked in a sharp fashion. They are not smeared over the mesh as in traditional Eulerian methods. Thus, materials can approach each other without mixing and a mixture formulation is not required in treating cells with multiple interfaces or in cells that are only partially filled. The exact interface location is known at all times due to the level set representation. Boundary conditions and jump conditions can be applied at the sharp interfaces at both free surfaces and material-material interfaces.
4. A particle-level set method [28] is used. This technique is shown to maintain sharp corners of objects without excessive smoothing due to the inherent entropy fix in the advection scheme used to evolve the narrow-band grid-based level set. Thus, spurious mass loss effects due to stretching and shearing of interfaces that plague all Eulerian interface tracking schemes are avoided in the present method. No difficulty arises in treating multiple boundaries. These are simply evolved as different level set functions. The interfaces can undergo topological changes without occasioning difficulties for the flow solver.
5. Extension to three dimensions should be straightforward. The numerical schemes for the governing equations are obtained by field-by-field decomposition along each dimension and therefore addition of the third dimension will only necessitate discretization of the equations in that direction. Furthermore, the level set formulation is also easily extended to three dimensions, thus allowing for tracking of three-dimensional objects as a straightforward extension of the technique presented in this work.

The method is benchmarked in this work by comparing with solutions using moving FEM techniques and experimental data.

2. Formulation of the problem

2.1. Constitutive relations

The equations governing the material deformation appropriate for high strain rate applications can be formulated by assuming that the volumetric or dilatational response is governed by an equation of state while the deviatoric response obeys a conventional flow theory of plasticity. The system of equations describing the material deformation in Lagrangian form can be written as follows. The stress in the material is expressed as the sum of the dilatational and deviatoric parts:

$$\sigma_{ij} = s_{ij} - p\delta_{ij}. \tag{1}$$

Here, σ_{ij} is the Cauchy stress tensor, s_{ij} its deviatoric part, and p the hydrostatic pressure taken to be positive in compression.

The rate of change of deviatoric stress is given by:

$$\overset{\nabla}{s}_{ij} = 2G(\bar{D}_{ij} - D^{\mathrm{p}}_{ij}), \tag{2}$$

$$\overset{\nabla}{s}_{ij} = \dot{s}_{ij} + s_{ik}\Omega_{kj} - \Omega_{ik}s_{kj}, \tag{3}$$

where G is the shear modulus, $\overset{\nabla}{s}_{ij}$ the Jaumann derivative, $\dot{s}_{ij}$ the total derivative of s_{ij}, $\bar{D}_{ij}$ the deviatoric strain-rate, D^{p}_{ij} the plastic strain-rate, and Ω_{ij} the spin tensor. The Jaumann derivative is used to ensure material frame indifference with respect to rotation.

The spin tensor and the strain-rate tensor are given by:

$$\Omega_{ij} = \tfrac{1}{2}(v_{i,j} - v_{j,i}), \tag{4}$$

$$D_{ij} = \tfrac{1}{2}(v_{i,j} + v_{j,i}), \tag{5}$$

where $D_{ij} = D^{\mathrm{e}}_{ij} + D^{\mathrm{p}}_{ij}$ is the strain-rate tensor composed of the elastic strain rate D^{e}_{ij} and the plastic strain rate D^{p}_{ij}, v_i is the ith velocity component, and $v_{i,j} = \partial v_i/\partial x_j$.

The deviatoric strain-rate is

$$\bar{D}_{ij} = D_{ij} - \tfrac{1}{3}D_{kk}\delta_{ij}. \tag{6}$$

The plastic strain-rate follows the relationships:

$$\mathrm{tr}(D^{\mathrm{p}}_{ij}) = 0, \tag{7}$$

$$D^{\mathrm{p}}_{ij} = \Lambda N_{ij}, \tag{8}$$

where $N_{ij} = s_{ij}/\sqrt{s_{kl}s_{kl}}$ is the unit outward normal to the yield surface and Λ a positive parameter called the consistency parameter.

The effective stress (S_{e}) and effective plastic strain ($\bar{\varepsilon}^{\mathrm{p}}$) are given by:

$$S^2_{\mathrm{e}} \equiv \tfrac{3}{2}\mathrm{tr}(s_{ij}s_{ji}), \tag{9}$$

$$\left(\dot{\bar{\varepsilon}}^{\mathrm{p}}\right)^2 = \tfrac{2}{3}\mathrm{tr}(D^{\mathrm{p}}_{ij}D^{\mathrm{p}}_{ij}). \tag{10}$$

The evolution of the temperature due to heat conduction and thermal energy produced by work done during elasto-plastic deformation is written as:

$$\rho C\dot{T} = k\nabla^2 T - \alpha(3\lambda + 2\mu)T_0\dot{\varepsilon}^{\mathrm{e}}_{kk} + \beta\dot{W}_{\mathrm{p}}, \tag{11}$$

where T is the temperature, C the specific heat, k the thermal conductivity, α the thermal expansion coefficient, λ and μ are the Lamé constants, β the Taylor–Quinney parameter implies the fraction of mechanical power convert to thermal power [29], and is taken as 0.9, and the stress power due to plastic work, $\dot{W}_{\mathrm{p}} \cong \dot{\bar{\varepsilon}}^{\mathrm{p}} S_{\mathrm{e}}$. For the applications considered in this work, the conduction and elastic work terms are small compared to the plastic work term.

The material models used in this work are rate-independent (Prandtl–Reuss material) and shear rate- and temperature-dependent [30] models, given (respectively) in general form as:

$$\sigma_{\mathrm{y}} = A + B(\bar{\varepsilon}^{\mathrm{p}})^n, \tag{12}$$

$$\sigma_{\mathrm{y}} = (A + B(\bar{\varepsilon}^{\mathrm{p}})^n)\left(1 + C\ln\left(\frac{\dot{\bar{\varepsilon}}^{\mathrm{p}}}{\dot{\varepsilon}_o}\right)\right)(1 - \theta^m). \tag{13}$$

Here, A, B, C, n, m, $\dot{\varepsilon}_o$ are model constants and $\theta = (T - T_0)/(T_{\mathrm{m}} - T_0)$, where T_0 and T_{m} are reference room temperature and melting temperature, respectively. In the Johnson–Cook model (Eq. (13)), the flow stress, σ_{y}, increases with an increase in the effective plastic strain and the effective plastic strain-rate and decreases with an increase in temperature. The yield stress in fact goes to zero as the temperature approaches the melting temperature of the material.

2.2. Governing equations

In the Eulerian setting, since material points are not followed, the above constitutive equations need to be combined with calculations of the flow of material. The equations governing axisymmetric deformation and flow of the material can be written as a system of conservation laws using the primitive variables as:

$$\frac{\partial\vec{Q}}{\partial t} + \frac{\partial F(\vec{Q})}{\partial x} + \frac{\partial G(\vec{Q})}{\partial y} = S(\vec{Q}), \tag{14}$$

where the vector of conserved variables ($\vec{Q}$) and the convective flux vectors in the x(radial)- and y(axial)-directions ($F(\vec{Q})$ and $G(\vec{Q})$) are:

$$\vec{Q} = \begin{Bmatrix} \rho \\ \rho u \\ \rho v \\ E \\ \rho s_{xx} \\ \rho s_{yy} \\ \rho s_{xy} \end{Bmatrix}, \quad F(\vec{Q}) = \begin{Bmatrix} \rho u \\ \rho u^2 + p \\ \rho uv \\ u[E + p] \\ \rho u s_{xx} \\ \rho u s_{yy} \\ \rho u s_{xy} \end{Bmatrix}, \quad G(\vec{Q}) = \begin{Bmatrix} \rho v \\ \rho uv \\ \rho v^2 + p \\ v[E + p] \\ \rho v s_{xx} \\ \rho v s_{yy} \\ \rho v s_{xy} \end{Bmatrix}. \tag{15}$$

The above equations, written in conservative form, include the evolution of the deviatoric stresses according to Eq. (2). The dilatational part of the stress (pressure) is obtained from an equation of state. The source vector that appears in Eq. (14) is of the form:

$$S(\vec{Q}) = \begin{Bmatrix} -\phi\frac{\rho u}{x} \\ \frac{\partial s_{xx}}{\partial x} + \frac{\partial s_{xy}}{\partial y} + \phi\left(\frac{s_{xx}+s_{yy}+s_{xy}}{x} - \frac{\rho u^2}{x}\right) \\ \frac{\partial s_{xy}}{\partial x} + \frac{\partial s_{yy}}{\partial y} + \phi\left(\frac{s_{xy}}{x} - \frac{\rho uv}{x}\right) \\ S_E \\ S_{S_{xx}} \\ S_{S_{yy}} \\ S_{S_{xy}} \end{Bmatrix},$$

where

$$S_E = -\phi\left(\frac{u(E+p)}{x} + \frac{\left(us_{xx} + vs_{yy}\right)}{x}\right) + \frac{\partial}{\partial x}\left(us_{xx} + vs_{yy}\right) + \frac{\partial}{\partial y}\left(us_{xy} + vs_{yy}\right). \tag{16a}$$

For the deviatoric stress evolution equations, the source terms are as follows:

$$S_{s_{xx}} = s_{xx}\left(\frac{\partial u}{\partial x} + \frac{\partial v}{\partial y}\right) + 2\Omega_{xy}s_{xy} + 2G\left[\frac{\partial u}{\partial x} - \Sigma\right], \tag{16b}$$

$$S_{s_{yy}} = s_{yy}\left(\frac{\partial u}{\partial x} + \frac{\partial v}{\partial y}\right) + 2\Omega_{yx}s_{xy} + 2G\left[\frac{\partial v}{\partial y} - \Sigma\right], \tag{16c}$$

$$S_{s_{xy}} = s_{xy}\left(\frac{\partial u}{\partial x} + \frac{\partial v}{\partial y}\right) + \Omega_{xx}s_{xy} + \Omega_{xy}s_{yy} - \Omega_{xy}s_{xx} - \Omega_{yy}s_{xy} + 2G\left[\frac{1}{2}\left(\frac{\partial u}{\partial y} + \frac{\partial v}{\partial x}\right)\right], \tag{16d}$$

where

$$\Sigma = \frac{1}{3}\left(\frac{\partial u}{\partial x} + \frac{u}{x} + \frac{\partial v}{\partial y}\right)$$

and $\phi = 0$ or 1 for the two-dimensional or two-dimensional-axisymmetric formulations, respectively.

The equation for evolution of the plastic strain and temperature fields are also solved to deduce the thermo-mechanical effects of the multimaterial interactions. These are written as:

$$\frac{\partial \bar{\varepsilon}^{\mathrm{p}}}{\partial t} + \vec{V}\cdot\nabla\bar{\varepsilon}^{\mathrm{p}} = \sqrt{\frac{2}{3}\mathrm{tr}(D^{\mathrm{p}}_{ij}D^{\mathrm{p}}_{ij})}, \tag{17}$$

$$\frac{\partial T}{\partial t} + \vec{V}\cdot\nabla T = \frac{1}{\rho C}\left(k\nabla^2 T - \alpha(3\lambda+2\mu)T_0\dot{\varepsilon}^{\mathrm{e}}_{kk} + \beta\dot{W}_{\mathrm{p}}\right). \tag{18}$$

The eigenvalues of the equation system (14) were found to be real [27] for the range of parameters, i.e., material properties and impact velocities of interest in this work. For one-dimensional formulation, the eigenvalues were shown to be [31]:

$$\lambda_1 = \lambda_2 = \lambda_3 = u, \tag{19a}$$

$$\lambda_4 = c + u, \tag{19b}$$

$$\lambda_5 = c - u. \tag{19c}$$

The sound speed depends on the particular equation of state chosen for the pressure and is given below for the case of the Mie–Grüneisen equation of state.

The above system of equations are first solved using the essentially non-oscillatory (ENO) numerical scheme [32,33] as will be described in a subsequent section. The radial return algorithm is then applied to bring the stress state back to the yield surface if the predicted von Mises stress falls outside the admissible states. Eqs. (17) and (18) for the effective plastic strain and temperature field are solved separately using a simple second-order upwind scheme.

2.3. Mie–Grüneisen e.o.s. for solids

It is necessary to relate pressure, specific volume, and internal energy through an equation of state in order to close the system of equations above. The overall pressure in a solid may be expressed as a sum of two terms, the first due to the thermal excitation and the second due to the pressure resulting from the attractive/repulsive forces in the lattice of atoms. For the present work, due to the high strain-rate, large deformation problem of concern, we utilize the Mie–Grüneisen e.o.s. If e_c and p_c denote, respectively, the "cold" (at 0 K) energy and pressure, the incomplete, temperature-independent formulation of the Mie–Grüneisen e.o.s. is

$$p(e,V) \sim \Gamma(V)\frac{(e-e_c(V))}{V} + p_c(V) = \Gamma\frac{e}{V} + f(V), \tag{20}$$

where, by definition,

$$e = \frac{E}{\rho} - \frac{u^2}{2}, \tag{21}$$

$$V = \frac{1}{\rho}, \tag{22}$$

and the Grüneisen parameter is defined as

$$\Gamma = V\left(\frac{\partial p}{\partial e}\right)_V = \frac{\Gamma_0\rho_0}{\rho}, \tag{23}$$

where ρ_0 is the density of the unstressed material, c_0 and s are coefficients that relate the shock speed U_s and the particle velocity u_p. Experiments on solids provide a relation between U_s and u_p [34]. A first approximation consists of a linear relation (generally applicable for strong shocks):

$$U_s = c_0 + su_p, \tag{24}$$

where c_0 is the bulk sound speed for the material at rest and s is related to the isentropic pressure derivative of the isentropic bulk modulus. In general, c_0 and s are obtained from experiments.

The expression for the sound speed is given by:

$$c^2 = \left(\frac{\partial p}{\partial \rho}\right)_e + \frac{p}{\rho^2}\left(\frac{\partial p}{\partial e}\right)_\rho = \Gamma e + f'(V) + \Gamma\frac{p}{\rho}. \tag{25}$$

For low energy and low pressure (as in a rarefaction), round-off and approximation errors may result in negative values of c^2, since f' changes sign. To correct this, and following the approach by Miller and Puckett [25], Arienti et. al. [23] prolong the e.o.s. with a pseudo elastic-solid e.o.s. The final expression for $f(V)$, to accommodate for negative pressure (tension) and preserve positive sound speed-squared, is written as:

$$f(V) = \begin{cases} \frac{\rho_0 c_0^2 \varphi}{(1-s\varphi)^2}\left[1 - \frac{\Gamma}{2V}(V_0 - V)\right] & \text{if } V \leqslant V_0, \\ c_0^2\left(\frac{1}{V} - \frac{1}{V_0}\right) & \text{if } V > V_0, \end{cases} \tag{26}$$

where $\varphi = 1 - (V/V_0)$.

2.4. Radial return algorithm

When a material deforms plastically, the set of stresses marking the transition boundary between the admissible and the inadmissible stress states is defined by the yield surface. The stress must be constrained to always fall either within or on the yield surface. Typically, numerical solutions of the plasticity equations tentatively assume that the material response for the entire time increment is purely elastic. If the resulting "predicted" or "trial" updated stress is found to fall outside the yield surface, then the numerical algorithm recognizes that the tentative assumption of elasticity must have been wrong. Classical return algorithms assert that the correct updated stress can be obtained by projecting the inadmissible trial stress back to the yield surface. There are various methods by which such return of the stress to the yield surface can be effected [35–37]. Here, we adopt an algorithm due to Ponthot [38].

We assume the existence of a general yield function f given, for a J_2 von Mises material with isotropic hardening, by:

$$f(s_{ij}, S_e) = S_e - \sigma_v, \tag{27}$$

where σ_v is the current yield stress.

The admissible stress states are constrained to remain on or within the domain defined by this yield function, i.e., we require that $f \leqslant 0$. The hardening law is given by:

$$\dot{\sigma}_v = \sqrt{\frac{2}{3}} h \Lambda, \tag{28}$$

where h is called the hardening coefficient and corresponds to the slope of the effective stress versus effective plastic strain curve under uniaxial loading conditions. Substitution of Eq. (8) into Eq. (10) results in $\dot{\bar{\varepsilon}}^p = \sqrt{2/3}\Lambda$. Eq. (28) can also be written as:

$$\dot{\sigma}_v = h\dot{\bar{\varepsilon}}^p, \tag{29}$$

which clearly indicates the role of the hardening coefficient. Time integration of the deviatoric stress equation for elasto-plastic deformations, i.e.,

$$\dot{s}_{ij} + s_{ik}\Omega_{kj} - \Omega_{ik}s_{kj} = 2G(\bar{D} - D^p) \tag{30}$$

is split into two parts, the elastic predictor which yields a trial stress assuming purely elastic deformation of the material,

$$\dot{s}_{ij,\mathrm{tr}} + s_{ik,\mathrm{tr}}\Omega_{kj} - \Omega_{ik}s_{kj,\mathrm{tr}} = 2G\bar{D}, \tag{31a}$$

and the plastic corrector to bring the computed trial stress back to the yield surface,

$$\dot{s}_{ij,\mathrm{cor}} = -2GD^p = -2G\Lambda N_{ij}, \tag{31b}$$

where the subscript tr is for trial, and cor is for correction. Note that the update of the deviatoric stress in Eq. (31a) is reflected in the source terms in Eqs. (16b)–(16d). Following the update using the system of equations in Eq. (14), the correction of the deviatoric stresses through the radial return is performed using Eq. (31b). The unit normal to the yield surface is approximated as:

$$N_{ij,\mathrm{tr}} = \frac{s_{ij,\mathrm{tr}}}{\sqrt{s_{kl,\mathrm{tr}} s_{kl,\mathrm{tr}}}}. \tag{32}$$

The return is effected in a direction normal to the yield surface as follows:

$$s_{ij,\mathrm{cor}} = s_{ij,\mathrm{tr}} - 2G\xi N_{ij,\mathrm{tr}}, \tag{33}$$

$$\bar{\varepsilon}_1^{\mathrm{p}} = \bar{\varepsilon}_0^{\mathrm{p}} + \sqrt{\tfrac{2}{3}}\xi, \tag{34}$$

where the unknown scalar parameter $\xi = \int_{t_0}^{t_1} \Lambda \, \mathrm{d}t$ where t_0 and t_1 are the beginning and end of the time interval of integration. This parameter is determined by the enforcement of the consistency condition, $f = 0$, at time $t = t_1$, i.e., we require that

$$f = \sqrt{\tfrac{3}{2}\left[s_{ij,\mathrm{tr}} - 2G\xi N_{ij,\mathrm{tr}}\right]\left[s_{ij,\mathrm{tr}} - 2G\xi N_{ij,\mathrm{tr}}\right]} - \sigma_v^1 = 0. \tag{35}$$

Eq. (35) can be solved for ξ by first discretizing Eq. (28) in time as

$$\frac{\sigma_v^1 - \sigma_v^0}{\Delta t} = \sqrt{\tfrac{2}{3}} h \Lambda, \tag{36}$$

where superscripts 0 and 1 denote the values at t_0 and t_1, respectively. Substituting for σ_v^1 using Eq. (36) into Eq. (35) and solving for ξ, one obtains the final expression:

$$\xi = \frac{\sqrt{s_{ij,\mathrm{tr}} s_{ij,\mathrm{tr}}} - \sqrt{2/3}\sigma_v^0}{2G\left(1 + \frac{h}{3G}\right)}. \tag{37}$$

Thus, once ξ is obtained, the correction of the predicted deviatoric stresses is performed using Eq. (31b) and the consistency condition is enforced.

3. Numerical method

3.1. Local Lax–Friedrichs essentially non-oscillatory (LLF-ENO) scheme

To solve the hyperbolic system of equations in one and two dimensions, the ENO shock-capturing scheme [32,33] is used. The Convex ENO scheme due to [39] is implemented, to enable the oscillation-free solution of the two-dimensional equations without field-by-field decomposition in the presence of large gradients. The discretization has been described in detail in a previous paper [27] and is only briefly outlined below.

Consider the governing equation for one-dimensional transport:

$$\frac{\partial \vec{Q}}{\partial t} + \frac{\partial F(\vec{Q})}{\partial x} = S(\vec{Q}). \tag{38}$$

Let

$$\frac{\partial \vec{Q}}{\partial t} = L(\vec{Q}), \tag{39}$$

where

$$L(\vec{Q}) = -\frac{F_e - F_w}{x_e - x_w} + D(\vec{Q}). \tag{40}$$

F_e and F_w are the fluxes at the east and west faces shown and x_e and x_w are the locations of the east and west faces, respectively, as shown in Fig. 1(a). D is an appropriate discrete operator for the source terms. In the current work, the source terms are discretized using a second-order central difference scheme. This was found to be robust for the calculations performed. However, it may be necessary in future work to develop a more sophisticated differencing procedure for the source terms as well.

The three-step third-order in time Runge–Kutta scheme is used in this work and takes the form [32,33]:

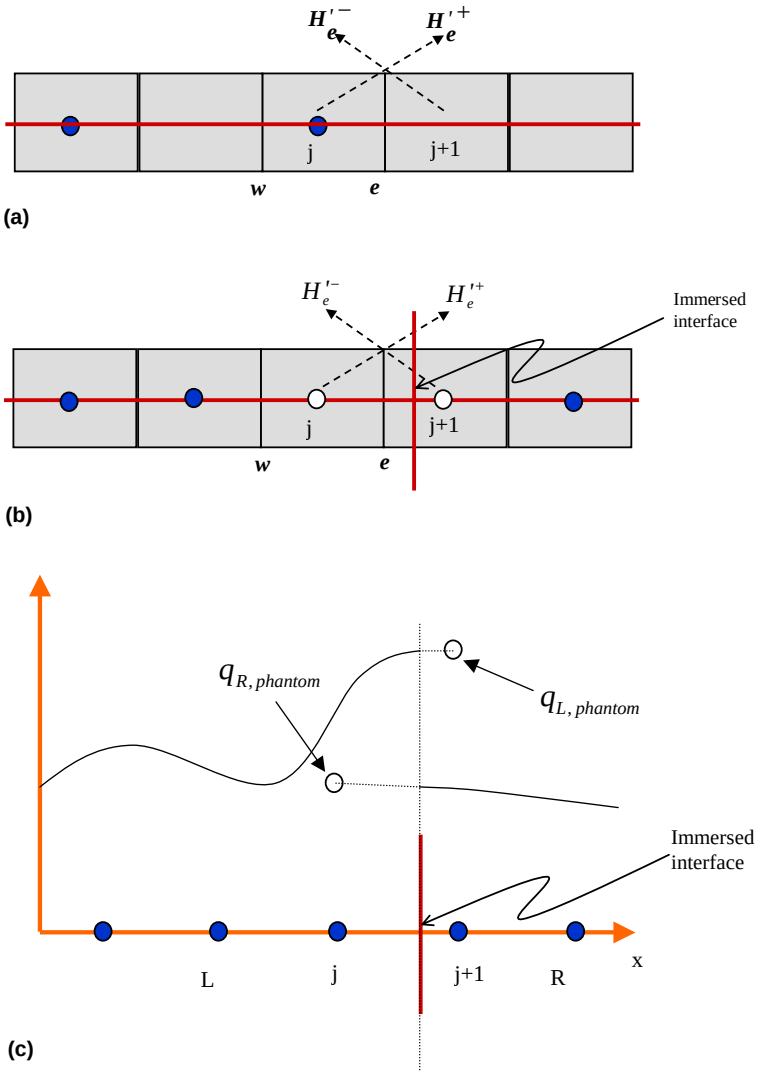

Fig. 1. (a) Illustration of grid point and grid face definitions for discretization of governing equations. H'^{+} and H'^{-} are derivatives of the interpolating function evaluated from the left and right stencils respectively. (b) Grid point and grid face definitions for evaluation of fluxes in the presence of an immersed boundary. (c) Example of profile of q variable along x.

$$\begin{aligned}\vec{Q}^{(1)} &= \vec{Q}^{(n)} + \Delta t L(\vec{Q}^{(n)}),\\ \vec{Q}^{(2)} &= \tfrac{1}{4}(\vec{Q}^{(1)} + 3\vec{Q}^{(n)}) + \tfrac{1}{4}\Delta t L(\vec{Q}^{(1)}),\\ \vec{Q}^{(n+1)} &= \tfrac{1}{3}(2\vec{Q}^{(2)} + \vec{Q}^{(n)}) + \tfrac{2}{3}\Delta t L(\vec{Q}^{(2)}).\end{aligned} \tag{41}$$

The spatial order of accuracy of the ENO formulation used to solve Eq. (38) is determined by the interpolation practices used to evaluate the fluxes at the faces e and w, i.e., in obtaining F_e and F_w in Eq. (40). Due to the presence of immersed boundaries, as illustrated in Fig. 1(b), care must be taken in computing these fluxes. The flux evaluations for the ENO formulation comes from derivatives of an interpolating function $H(x)$ as follows:

$$F_e = \frac{d}{dx}[H(x)]_{x=x_e}. \tag{42}$$

The derivatives are evaluated from divided differences and the flux evaluation is performed as follows:

$$F_e = F_e^+ + F_e^- = H'^+(x_e) + H'^-(x_w). \tag{43}$$

The superscripts (+) and (−) indicate the positive and negative direction fluxes at the face e under consideration as illustrated in Fig. 1(a). The derivatives H' are obtained by polynomial reconstruction of the fields as in the standard ENO implementations. The present formulation based on the Convex ENO scheme proposed by Liu and Osher [39] chooses the divided difference value "closest" to the previous order flux chosen. The scheme reduces to low-order automatically at discontinuities, while maintaining higher-order in smooth regions. The first divided difference is obtained as follows:

$$H'^+(x_e) = H^+\left[x_{j-\frac{1}{2}}, x_e\right] = \frac{1}{2}\left(f(q[x_j]) + \alpha_{j+\frac{1}{2}} q\left[x_j\right]\right) \tag{44a}$$

and

$$H'^-(x_e) = H^-\left[x_e, x_{j+\frac{3}{2}}\right] = \frac{1}{2}\left(f(q[x_{j+1}]) - \alpha_{j+\frac{1}{2}} q\left[x_{j+1}\right]\right), \tag{44b}$$

where $\alpha_{j+1/2}$ is the characteristic speed evaluated at the cell face location $x_{j+1/2}$. This is evaluated as the maximum eigenvalue of the set in Eq. (38) at the cell face.

For points that are adjacent to the immersed interface such as j in Fig. 1(b), the flux evaluations need to be modified. Here, the east face is still taken at the grid cell face and for point j:

$$H'^+(x_e) = H\left[x_{j-\frac{1}{2}}, x_e\right] = \frac{1}{2}(f(q[x_j]) + \alpha_{j+\frac{1}{2}} q\left[x_j\right]), \tag{45a}$$

$$H'^-(x_e) = H\left[x_e, x_{j+\frac{3}{2}}\right] = \frac{1}{2}(f(q_{ghost}) - \alpha_{j+\frac{1}{2}} q_{ghost}), \tag{45b}$$

where q_{ghost} is the ghost value of the convected scalar variable q (see Fig. 1(c)). This value needs to be obtained while satisfying appropriate boundary conditions on the immersed interface as described below. This type of interfacial flux treatment of course reduces the order of accuracy at the immersed boundaries by one order. However, the high-order scheme is retained in the bulk of the computational domain. Similar considerations apply in the Ghost Fluid Method [26] for multifluid interactions and flux separation method [40] for the treatment of shock and contact discontinuities.

3.2. Boundary conditions

To evaluate the fluxes in the discrete form as in Eq. (40), appropriate boundary conditions need to be applied at the interface location. As can be seen in Fig. 2(a), when two interfaces collide a portion of an interface in the material–material contact region can have an immediately adjoining portion that falls in the material–void region of the interface. At each instant of the interface deformation, the ghost points (defined as points which are immediately outside a given body as indicated in Fig. 2(b)) associated with each portion of the interface have to be classified as collision (material–material or M–M) or free (material–void or M–V) ghost points and the appropriate b.c.s applied at the interfaces by supplying values to the ghost points. The procedure for determining how a ghost point of an interface is to be classified as collision or free ghost point is discussed in Section 4.3.

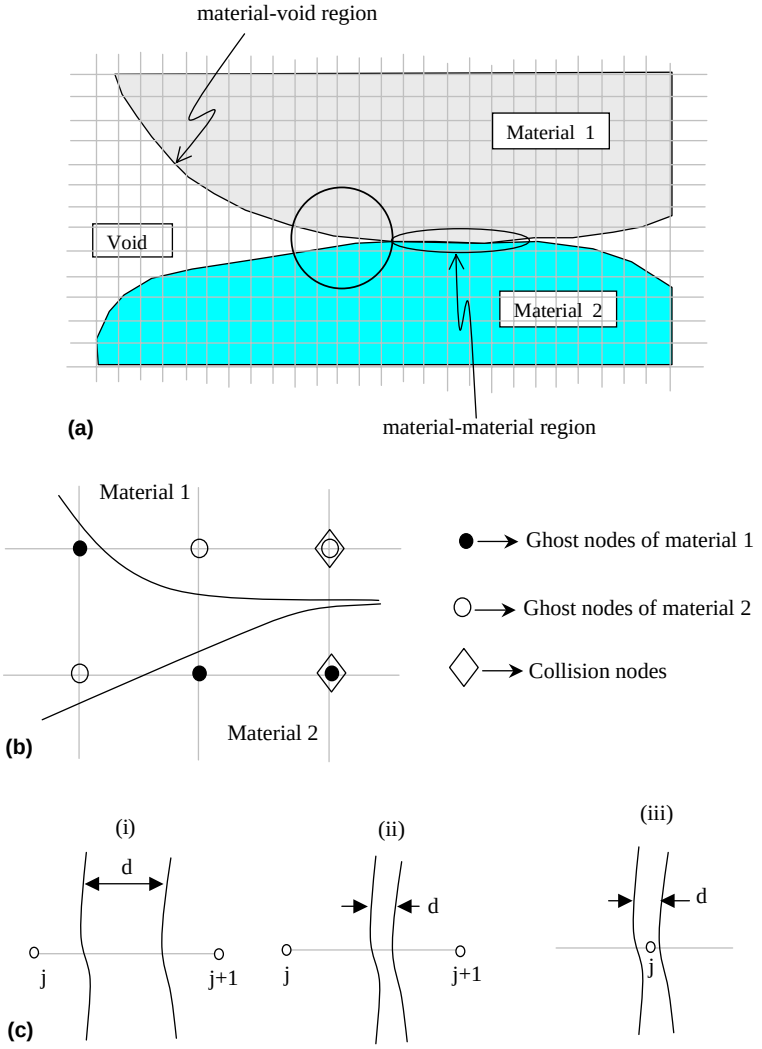

Fig. 2. (a) Illustration of boundary types when multiple bodies interact. (b) Zoom-in view of two bodies in contact show ghost and collision nodes. (c) Collision scenarios of two bodies in one dimension.

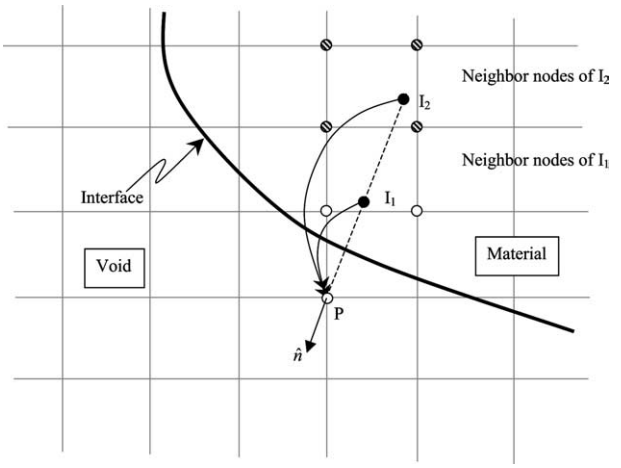

Fig. 3. Illustration of extrapolation process.

At the outset, all the dependent variables are extrapolated from the interior of a material to the ghost points. Thereafter, depending on the boundary conditions, these extrapolated values are replaced by values that satisfy the boundary conditions at the boundary of the material in question. Therefore, before discussing the boundary conditions, it is useful to outline the procedure for extrapolating values from the interior of a given material to ghost points lying across the boundary of the material. In order to extrapolate values from an object to the ghost point P, as illustrated in Fig. 3, the ghost point at P is first reflected (along the local normal obtained from the level set field) across the material interface. The values of all the dependent variables at the mirror point I_1 are then determined by interpolation from the surrounding nodes. Care is exercised to ensure that there are four immediate surrounding nodes lie in the same phase in which point I_1 resides. If this is the case, then bilinear interpolation procedure can be carried out in a straightforward way to obtain values for point I_1. A second point, point I_2 in Fig. 3, is also placed at a distance $dl = \sqrt{\Delta x^2 + \Delta y^2}$ from point I_1 (Fig. 3) along the normal from ghost point P to the interface. Again bilinear interpolation is employed to obtain values for point I_2 if there exist four immediate neighboring nodes in the same phase. If all four of the surrounding points are not in the same material for either point I_1 or I_2, then distance-weighted interpolation from the surrounding grid points that lie in the same phase is performed to obtain values for that point. Using values at points I_1 and I_2, linear extrapolation is then performed to obtain values for the ghost point P. Initially all the dependent variables are extrapolated to the ghost points. These values are then replaced as described below depending on the type of boundary condition to be applied on the interface adjoining the ghost point.

3.2.1. Type 1: Material–material interface

Boundary conditions on portions of the interface which qualify as material–material interfaces are developed based on the physically imposed interface conditions. At a material–material (or collision) interface, we enforce continuous material point velocities normal to the interface for the two materials and the continuity of normal traction and temperature, whereas the tangential traction component may remain discontinuous. The procedure for applying the interface conditions is illustrated in Fig. 4(a), where the subscript A denotes object A and subscript B denotes object B. We want to determine the variables at point P_A (ghost point of A, which lies inside object B) by replacing the extrapolated values with ones that apply

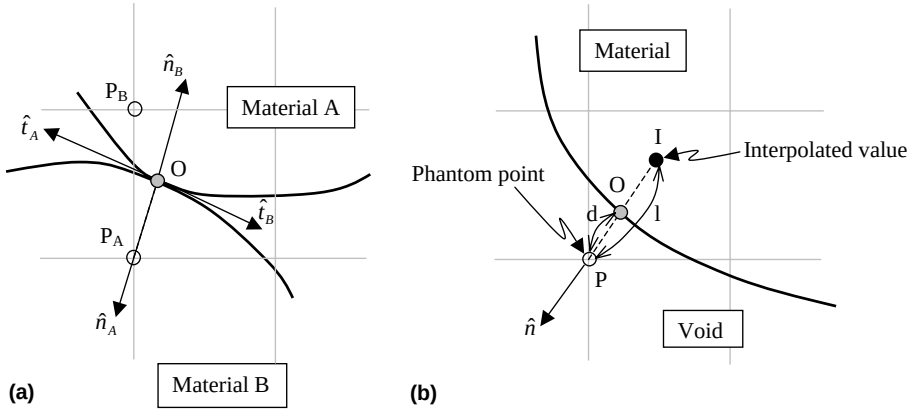

Fig. 4. Illustration of boundary conditions for (a) material–material boundaries and (b) material–void boundary.

the required boundary conditions at the interface location O shown in Fig. 4(a). First, the unit normal vector is computed at point P_A for object A using the level set field. The normal and tangential velocity components at point P_A are related to the x- and y-direction velocities as:

$$v_n = u_P n_x + v_P n_y, \tag{46a}$$

$$v_t = u_P n_y - v_P n_x. \tag{46b}$$

Since normal velocities are continuous across the interface, the value of the normal velocity component in Eq. (46a) is specified to be that of the object B at that point. The tangential velocity component in Eq. (46b) is assigned to be the extrapolated value from the material A. With these values of v_n and v_t, the Cartesian velocity components at the point P_A are then obtained from:

$$u_P = v_n n_x + v_t n_y, \tag{47a}$$

$$v_P = v_n n_y - v_t n_x. \tag{47b}$$

With the extrapolated values of ρ and E, pressure is obtained from equation of state.

The tangential, normal, and shear stresses at the ghost point P_A are computed such that the continuity of normal stress is enforced at the interface. The components of stress oriented with the local tangent and normal directions are computed from:

$$\sigma_{tt} = n_{x,A}^2 s_{yy,A} + n_{y,A}^2 s_{xx,A} - 2n_{x,A} n_{y,A} s_{xy,A} - p_{,A}, \tag{48a}$$

$$\sigma_{nn} = n_{x,A}^2 s_{xx,B} + n_{y,A}^2 s_{yy,B} + 2n_{x,A} n_{y,A} s_{xy,B} - p_{,B}, \tag{48b}$$

$$\sigma_{nt} = n_{x,A} n_{y,A} (s_{yy,B} - s_{xx,B}) + (n_{x,A}^2 - n_{y,A}^2) s_{xy,B}, \tag{48c}$$

where subscripts t and n denote tangent and normal directions to the interface at point O and subscripts A and B indicate the material from which the data are obtained. Note that in Eq. (48a), the tangential stress is computed using the extrapolated values of object A at P_A. This implies that the tangential stress remains discontinuous across the interface. In Eqs. (48b) and (48c), the normal and shear component stresses are

computed using field values of object B at P_A. This results in continuity of normal and shear stresses across the interface.

Converting to Cartesian coordinates, using Eqs. (48a)–(48c), the total stresses at the ghost point P_A of object A are obtained:

$$\sigma_{xx} = n_{x,A}^2\sigma_{nn} + n_{y,A}^2\sigma_{tt} - 2n_{x,A}n_{y,A}\sigma_{nt}, \tag{49a}$$

$$\sigma_{yy} = n_{y,A}^2\sigma_{nn} + n_{x,A}^2\sigma_{tt} + 2n_{x,A}n_{y,A}\sigma_{nt}, \tag{49b}$$

$$\sigma_{xy} = n_{x,A}n_{y,A}(\sigma_{nn} - \sigma_{tt}) + (n_{x,A}^2 - n_{y,A}^2)\sigma_{nt}. \tag{49c}$$

Assuming continuity of the temperature at the interface between the materials, the value of temperature at P_A is assigned the value of temperature in object B at the grid point coincident with P_A. The value of equivalent plastic strain is extrapolated from the interior of object A.

When interface conditions are obtained as above at impact boundaries "overheating" of the material can result, as pointed out by Glaister [22]. The problem arises due to the collision of the impinging shock on a solid wall and the reflected shock coming off a solid wall [41]. The overshoots in the density and temperature are numerical artifacts that arise due to the unphysical dissipation inherent in the numerical schemes and the inability of the Euler equations to conduct heat away from the overheated region into the wall thus causing a buildup of temperature [42]. Pressure and velocity appear to equilibrate quickly but internal energy (temperature) does not and the use of the e.o.s. renders the density value inaccurate also. This problem has been shown in a previous paper [27] to exist in both Eulerian and Lagrangian computations of impact. A fix for this problem has been suggested by Fedkiw et al. [43] for the case of gases and other materials. In the present computations with solids this fix has not been applied since further examination of this condition is required to determine its suitability to materials with strength, since the pressure in the present case is also related to the stresses in the material.

3.2.2. Type 2: Material–void interface

For a material–void interface, the physically imposed conditions on the interface are that the surface tractions be negligible. Therefore

$$\vec{n} \cdot (-pI + T) = 0, \tag{50}$$

where I is the unit tensor and T is the deviatoric stress tensor. In the one-dimensional case, the zero traction condition reduces to

$$\sigma_x^{\pm} = (s_x - p)^{\pm} = 0. \tag{51}$$

This condition is easily applied at the material–void interface in one-dimensional for the independent variable s_x at the interface, since the pressure is given by the equation of state.

In the two-dimensional case, implementation of this boundary condition requires care. To apply the zero-traction condition, we first rotate the stress tensor as follows. Let

$$\hat{\sigma} = A^{\mathrm{T}}\sigma A, \tag{52}$$

where

$$\hat{\sigma} = \begin{bmatrix} \sigma_{nn} & \sigma_{nt} \\ \sigma_{tn} & \sigma_{tt} \end{bmatrix} \quad \text{and} \quad A = \begin{bmatrix} n_x & -n_y \\ n_y & n_x \end{bmatrix}$$

are the rotated stress and orientation matrices due to the transformation from x–y to t–n coordinates, the latter coordinates having axes oriented along the tangent and normal to the interface. The physical

conditions at the interface require that the normal and shear components of traction be zero, while the tangential component may remain discontinuous. As illustrated in Fig. 4(b), we first compute the unit normal vector at the ghost point P (which lies in the void) from the level set field. The reflection of point P across the interface lies inside the material at point I. Expanding Eq. (52), the stresses oriented along the normal and tangent at P are obtained at the point I by interpolation from:

$$\sigma_{\mathrm{nn},I} = n_x^2 s_{xx,I} + n_y^2 s_{yy,I} + 2n_x n_y s_{xy,I} - p_{,I}, \tag{53a}$$

$$\sigma_{\mathrm{nt},I} = (n_x^2 - n_y^2) s_{xy,I} + n_x n_y (s_{yy,I} - s_{xx,I}). \tag{53b}$$

Since the values at the interface for all tractions are zero for σ_{nn} and σ_{nt}, linear extrapolation is performed to obtain the σ_{nn} and σ_{nt} at point P, using the values at I given by Eqs. (53a), (53b) and the interfacial values. If the distance between point E and the interface is less than a certain tolerance (here, we use $0.1 \times \min(\Delta x, \Delta y)$), then σ_{nn} and σ_{nt} are then taken to be zero at the point P. If not, then:

$$\sigma_{\mathrm{nn},P} = -\frac{l}{d}\sigma_{\mathrm{nn},I}, \tag{54a}$$

$$\sigma_{\mathrm{nt},P} = -\frac{l}{d}\sigma_{\mathrm{nt},I}. \tag{54b}$$

The stress component σ_{tt} is not required to be continuous across the interface and is obtained using the extrapolated ghost values at P:

$$\sigma_{\mathrm{tt},P} = n_x^2 s_{yy,P} + n_y^2 s_{xx,P} - 2n_x n_y s_{xy,P} - p_{,P}. \tag{55}$$

Converting to Cartesian components, from Eqs. (54a), (54b) and (55), the stresses at the ghost point P are obtained from:

$$\sigma_{xx,P} = n_x^2 \sigma_{\mathrm{nn},P} - 2n_x n_y \sigma_{\mathrm{nt},P} + n_y^2 \sigma_{\mathrm{tt},P}, \tag{56a}$$

$$\sigma_{yy,P} = n_y^2 \sigma_{\mathrm{nn},P} + 2n_x n_y \sigma_{\mathrm{nt},P} + n_x^2 \sigma_{\mathrm{tt},P}, \tag{56b}$$

$$\sigma_{xy,P} = n_x n_y (\sigma_{\mathrm{nn},P} - \sigma_{\mathrm{tt},P}) + (n_x^2 - n_y^2)\sigma_{\mathrm{nt},P}. \tag{56c}$$

All other variables are extrapolated. Note that no boundary conditions are required on the void side of the interface since the equations are not solved in the void region.

4. Interface capturing scheme

Discontinuities in properties will typically exist across interfaces between interacting materials and will need to be maintained during their interactions. For example, the density and material strength properties across an interface could be different by several orders of magnitude (e.g., at an air-copper boundary). Traditional purely Eulerian numerical methods solve the governing equations by adopting the single domain approach, i.e., the same governing equations are solved at each node in the domain, whether void or material node. The embedded interfaces and accompanying discontinuities are then accounted for by using different techniques, including volume-averaging, mixture theories [44], or by using "numerical" delta or heaviside functions [45,46]. As an alternative to such Eulerian (diffuse interface) methods it is possible to

formulate a sharp-interface technique on fixed meshes. In sharp-interface approaches, accurately maintaining the physically expected sharp interfaces between materials requires sophisticated interface tracking methods and discretization schemes that account for the embedded sharp interfaces. Such approaches have been advanced recently by various researchers [26,27,40,47].

In a previous work [27], the interface was tracked explicitly using marker particles and parametrized curves. Such an approach can become complicated in a three-dimensional setting or when the interfaces undergo topological changes. An alternative is to track the interfaces implicitly over the mesh using the level set approach. The advantage of the level set approach is that while a purely Eulerian update is employed to advance the interface via the level set (distance function) representation, the exact location of the interface can be deduced from the level set field. Thus, the level set method is compatible with a sharp-interface treatment. Furthermore, the level set approach easily extends to three dimensions and can naturally handle merger/fragmentation of the interface. However, grid-supported level set methods build in an entropy condition that leads to smoothing of sharp corners (cusps) on the interface. While in most physical problems this feature of level set advection can be advantageous, as unphysical re-entrant interfaces are naturally avoided, in the cases of interest to the present work this aspect of the level set method proves to be a hindrance. This is because we wish to follow the dynamics of solid objects, which may possess corners and other geometric features which must be carried without deterioration over the mesh. Recently, a hybrid particle level set (HPLS) method was presented by Enright et al. [28], which allows transport of corners and other sharp geometric features without dissipation. This method is briefly described in the following section and the results from the calculations using the method demonstrate the usefulness and appropriateness of the method for the class of problems solved in the present study.

4.1. Level set method

In the present work a local-level set formulation is used to capture the moving boundaries on a fixed Cartesian computational grid. The method introduces a continuous scalar function $\Phi(\vec{x},t)$, where the position of the actual interface is identified by an iso-value of the field, i.e., $\Phi = 0$. If multiple objects are present, a separate level set function is used to describe each object.

The motion of the interface is determined by a velocity field $\vec{u}$, which can depend on position, time, and geometry of the interface. The motion of the interface can thus be described by a scalar convection equation:

$$\frac{\partial \Phi}{\partial t} + \vec{u} \cdot \nabla \Phi = 0. \tag{57}$$

Since we are only interested in the location of the interface $\Phi(\vec{x},t) = 0$, the above equation only needs to be solved locally near the interface [48,49]. Eq. (57) is integrated using fourth-order ENO scheme in space and a third-order Runge–Kutta scheme in time.

The unit normal on the interface, drawn from inside the material ($\Phi < 0$) to outside of the material ($\Phi > 0$), and the curvature of the interface can easily be expressed in terms of $\Phi(\vec{x},t)$,

$$\vec{n} = \left.\frac{\nabla \Phi}{|\nabla \Phi|}\right|_{\Phi=0} \quad \text{and} \quad \kappa = \nabla \cdot \left.\left(\frac{\nabla \Phi}{|\nabla \Phi|}\right)\right|_{\Phi=0}. \tag{58}$$

The standard reinitialization algorithm maintains the signed distance property by solving to steady state the equation:

$$\phi_\tau + \vec{w} \cdot \nabla \phi = \mathrm{sign}(\Phi), \tag{59}$$

where τ is the fictitious time,

$$\operatorname{sign}(\Phi) = \frac{\Phi}{\sqrt{\Phi^2 + (\Delta x)^2}} \quad \text{and} \quad \vec{w} = \operatorname{sign}(\Phi)\frac{\nabla\phi}{|\nabla\phi|}, \tag{60}$$

with the initial condition

$$\phi(\vec{x}, 0) = \Phi(\vec{x}). \tag{61}$$

However, due to the built-in dissipation in the ENO scheme and the reinitialization procedure, excessive regularization occurs at under-resolved regions. Thus, sharp corners are rounded off and objects may lose mass during large deformations. Introducing Lagrangian particles in combination with the grid-based level set can remedy this problem as shown by Enright et al. [28].

4.2. Hybrid particle level set method

The hybrid particle level set method [28] is the combination of an Eulerian level set method and particle-based Lagrangian scheme. The particles, of positive and negative type, are placed randomly near the interface, attracted to the correct side to the interface (positive for $\Phi > 0$ and negative for $\Phi < 0$) and passively advected with the flow using the equation:

$$\frac{\mathrm{d}\vec{x}_\mathrm{p}}{\mathrm{d}t} = \vec{u}(\vec{x}_\mathrm{p}), \tag{62}$$

where $\vec{x}_\mathrm{p}$ is the position of the particle, which is the center of a sphere of radius r_p and $\vec{u}(\vec{x}_\mathrm{p})$ is its velocity, obtained by bilinear interpolation of values on the mesh. This applies for particles in the void region as well because there exists a level set extension velocity field. Since this advection procedure entails no dissipation, the distance function values carried by the Lagrangian particles can be considered to be "correct". Thus, if the grid-based level set function differs in some region of the interface from the level set values carried by the particles, the grid-based level set function is taken to be in need of correction. Detailed implementation of the advection and book-keeping of the particles carrying the level-set field is discussed in the paper by Enright et al. [28].

While the particles do not have mass, they have volume. The radius of each particle is bounded by minimum and maximum values based upon grid spacing. The maximum and minimum radii which work well, according to Enright et al., are:

$$r_\mathrm{min} = 0.1\min(\Delta x, \Delta y, \Delta z), \tag{63}$$

$$r_\mathrm{max} = 0.5\min(\Delta x, \Delta y, \Delta z). \tag{64}$$

Initially particles of both signs are randomly placed within a band of $3 \times \max(\Delta x, \Delta y, \Delta z)$ of the interface. Particles are then attracted to the correct side of the interface (i.e., positive particles to the $\Phi > 0$ side and negative particles to the $\Phi < 0$ side). Finally, each particle radius is set according to:

$$r_\mathrm{p} = \begin{cases} r_\mathrm{max} & \text{if } s_\mathrm{p}\Phi(\vec{x}_\mathrm{p}) > r_\mathrm{max}, \\ s_\mathrm{p}\Phi(\vec{x}_\mathrm{p}) & \text{if } r_\mathrm{min} \leqslant s_\mathrm{p}\Phi(\vec{x}_\mathrm{p}) \leqslant r_\mathrm{max}, \\ r_\mathrm{min} & \text{if } s_\mathrm{p}\Phi(\vec{x}_\mathrm{p}) < r_\mathrm{min}. \end{cases} \tag{65}$$

The particles that escaped to the wrong side of the interface are used to locate possible errors in the level set function since the escaped particles indicate that the characteristics have most likely been incorrectly merged through regularization, i.e., the level set has computed an incorrect weak solution (see Fig. 5). Once errors are located, reduction of error is carried out to rebuild the grid-based level set at these local regions.

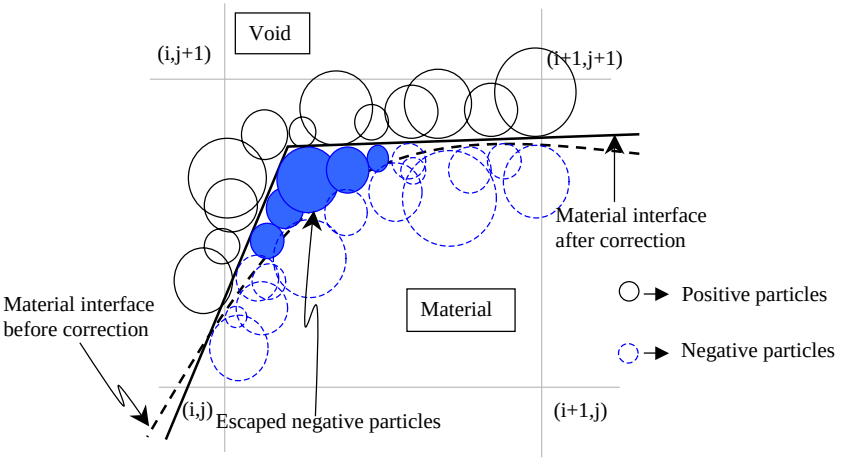

Fig. 5. Illustration of escaped negative particles used in error correction procedure.

The error correction procedure due to Enright et al. is as follows. Given a grid-based level set Φ identify the set of escaped positive particles E^+ (a escaped positive particle is defined as a positive type particle that happens to be located on the negative side of the grid level set as illustrated in Fig. 5). Initialize Φ^+ with Φ and then calculate,

$$\Phi^+ = \max_{\forall p \in E^+}(\Phi_p, \Phi^+), \tag{66}$$

where $\Phi_p(\vec{x})$ is defined as

$$\Phi_p(\vec{x}) = s_p\left(r_p - \left|\vec{x} - \vec{x}_p\right|\right) \tag{67}$$

and s_p is the sign of the particle.

Similarly, to calculate a reduced error presentation of the $\Phi \leqslant 0$ region, initialize Φ^- with Φ, then calculate,

$$\Phi^- = \min_{\forall p \in E^-}(\Phi_p, \Phi^-). \tag{68}$$

Φ^+ and Φ^- are then merged back into a single level set by setting Φ equal to the value of Φ^+ or Φ^- which is least in magnitude at each grid point,

$$\Phi = \begin{cases} \Phi^+ & \text{if } |\Phi^+| \leqslant |\Phi^-|, \\ \Phi^- & \text{if } |\Phi^+| > |\Phi^-|. \end{cases} \tag{69}$$

The minimum magnitude is used to reconstruct the interface, since it gives priority to values that are closer to the interface.

The above procedure for error correction was found to yield somewhat unsatisfactory results for certain types of rigid body motions when the meshes used were not sufficiently fine. When several field equations, such as in the present case, need to be solved simultaneously with the level-set equation, the grid sizes required to robustly track the sharp corners become rather prohibitive. A modification to the error correction procedure of Enright et al. was therefore made, as given below, which appears to be more robust (although somewhat more dissipative), based on test problems run using modest grid sizes.

Given a level-set function Φ and a set of escaped positive particles E^+, we initialize the corrected distance function values at the 4 surrounding grid points Φ^+ with Φ, the values obtained by advection of the grid-based level set, and then calculate:

$$\Phi^+ = \max_{\forall p \in E^+} \left(\left| \Phi_p \right|, |\Phi^+| \right) \quad \text{if } \Phi^+ > 0, \tag{70a}$$

$$\Phi^+ = -\min_{\forall p \in E^+} \left(\left| \Phi_p \right|, |\Phi^+| \right) \quad \text{if } \Phi^+ < 0. \tag{70b}$$

For all the escaped particles marked as positive type (Fig. 5), Eqs. (70a) and (70b) attempt to correct the interface location by computing new level set values at the four corners. This in effect moves the grid-based interface (i.e., the $\Phi = 0$ level) so that the escaped positive particle would be returned to the correct distance on the positive side of the interface. Similarly, a correction of the grid values can be applied in the correction procedure for the negative escaped particles. Thus, for a set of escaped negative particles E^-, we initialize Φ^- with Φ and then calculate

$$\Phi^- = \min_{\forall p \in E^-} \left(\left| \Phi_p \right|, |\Phi^-| \right) \quad \text{if } \Phi^- > 0, \tag{71a}$$

$$\Phi^- = -\max_{\forall p \in E^-} \left(\left| \Phi_p \right|, |\Phi^-| \right) \quad \text{if } \Phi^- < 0. \tag{71b}$$

The Φ^+ and Φ^- values are then merged back to obtain the distance function field Φ on the grid as described above.

4.3. Detecting and resolving collisions

In the present work, material interfaces are expected to collide with other interfaces or collapse and fragment. Such events need to be tracked and appropriate interface conditions applied on the interacting parts of the interfaces. In the current framework, multiple objects with different material properties are described by different level set functions. Only one material can possess a given computational grid point at any time, whether it be void or solid material.

The collision between various objects is determined by first defining the properties of each level set. Each level set (object) is associated with a set of grid points which straddle the object boundary, i.e., the zero-contour of the level-set. In two-dimensions, these grid points are identified as those across which the level set values change sign from negative to positive. Among this set, the grid points that lie within the material defined by that particular level set function are called "boundary" points and those lying just outside are classified as "ghost" points. This set of points is stored in a one-dimensional array, with mapping assigned to access the grid indexes. At any given time step, one can search through this set of grid points that straddle the zero-level for each object to determine whether these points are free boundary nodes or collision nodes as described below.

Various situations can arise when two different objects move toward each other as shown in Fig. 2(c, i–iii). The distance between two interfaces is easily computed using the level set functions associated with each interface. At any grid point, if we are solving for two level set functions, the values of each level set at that point represent the distance to their respective interfaces. Therefore, the sum of these values represents the distance between the two interfaces. If the distance between two approaching level sets is less than a specified tolerance, set to $0.1 \times \min(\Delta x, \Delta y)$, as in Fig. 2(c, ii and iii), then the ghost point is marked as a collision boundary point. If not (Fig. 2(c, i)), then the ghost point is marked as a free boundary point. This process is repeated for each level set after the calculation of the interface velocity for each level set. For the collision boundary nodes, each level set interface velocity must be corrected so that one object will not

penetrate the other. For two level sets, each defining a moving boundary under impending collision, the normal velocity at the interface is continuous through the impact surface, whereas the tangential component may be discontinuous as sliding is permitted. No surface friction is accounted for in this work but can easily be included in the present framework. If one level set is specified as moving boundary type and the other as rigid stationary boundary type, then the normal component of velocity is zero when two such interfaces collide.

Having marked the ghost points as collision or free boundary points, the boundary conditions can be applied at the interface locations as described in Section 3.2. The level set velocities are then obtained and the interfaces are advected to their new positions. After all the level set functions are evolved, we then again find a new set of ghost points and determine the collision nodes.

5. Results

The numerical scheme applied to evolve the flowfields through Eq. (14) has been tested for one-dimensional problems involving impact and deformation in previous work [27]. Here, we apply the scheme, in combination with the particle-level-set interface capturing method and the boundary treatments described in previous sections to two-dimensional problems. The results are compared with benchmark solutions and experimental data.

5.1. Two-dimensional axisymmetric Taylor impact of a copper rod

In the two-dimensional setting, we first validate the methods presented above by testing against the well known Taylor bar benchmark test [50]. A cylindrical rod made of copper with an initial radius of 3.2 mm and a length of 32.4 mm is given a velocity of 227 m/s (schematic shown in Fig. 6) and impacts against a

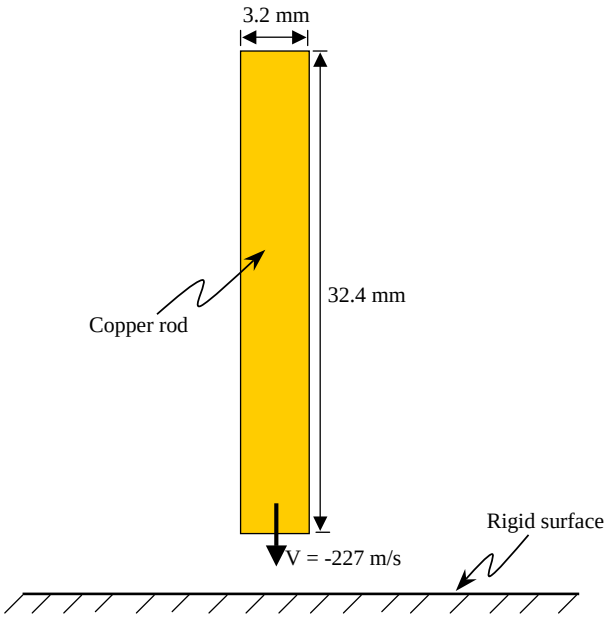

Fig. 6. Schematic of the Taylor bar impact problem.

rigid planar surface. The deformation of the rod is presumed to be axisymmetric. The rod has an initial density of 8930 kg/m^3, Young's modulus $E = 117$ GPa, Poisson's ratio $v = 0.35$, and yield stress $\sigma_y = 400$ MPa. The material is assumed to harden linearly with a plastic modulus of 100 MPa. The calculations are carried out up to a time of 80 μs, at which point nearly all the initial kinetic energy has been dissipated as plastic work [51].

Two level sets are initialized, one for the copper rod and the other for the rigid body. Since the bottom rigid body is not moving, there is no need to initialize it with particles. Therefore particles are seeded only for the copper rod. Collision between two bodies is detected using the algorithm discussed in Section 4.3, and the calculations are carried out with the material–material and material–void boundary conditions applying on the collision and free surfaces of the rod, as discussed in Section 3.2.

A grid independence study is performed using 20×100, 40×200, 60×300, and 80×400 meshes. Fig. 7 shows the final shapes (at 80 μs) for all the meshes mentioned. It is clear that the solution converges with grid refinement and grid-independent results are approached for the finest mesh, 80×400.

Fig. 8 shows the (grid-independent) solutions for the 80×400 mesh at four different times after impact, i.e., 20, 40, 60, and 80 μs. It can be observed that the rod initially extends out rapidly at the point of impact and continues to extend at the foot up to around 40 μs. As the material in the foot hardens, a second bulge is formed, extending out to approximately 0.004 m from the axis. The extent of the bulge, both in the radial

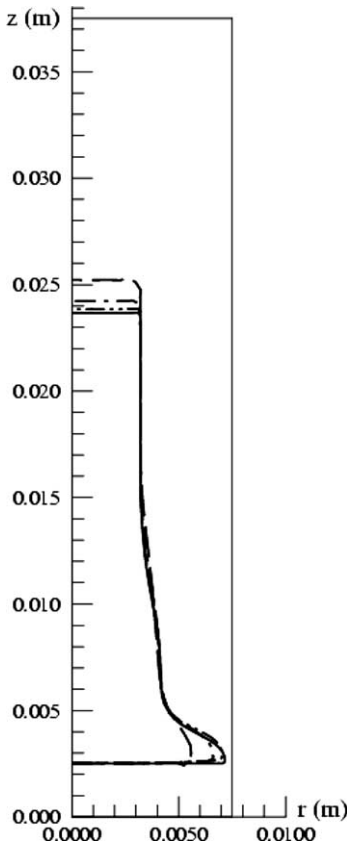

Fig. 7. Grid refinement study in Taylor bar impact calculation, with a velocity of 227 m/s. Final shapes of 20×100 mesh (– – –-), 40×200 mesh (-·-·-·-), 60×300 mesh (– · · – ··), and 80×400 mesh (——).

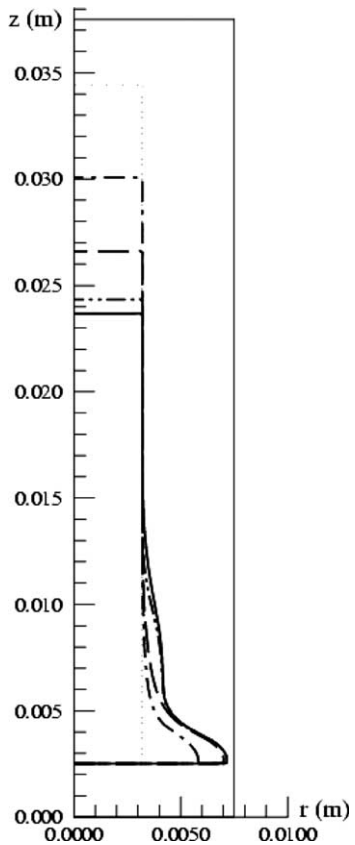

Fig. 8. Shapes of Taylor bar impact calculation at different times for 80×400 mesh, with a velocity of 227 m/s. At 20 μs (-·-·-·-), 40 μs (– – –-), 60 μs (– · · – – · ·), and 80 μs (——).

and longitudinal directions, is in excellent agreement with the results of Camacho and Ortiz [7]. The rod reaches a rest state around the time of 80 μs in agreement with Camacho and Ortiz, showing that the conversion of kinetic energy to plastic work is correctly predicted.

The numerical values for final rod length, radius, and maximum equivalent plastic strain are compared with other results in literature in Table 1. Our results fall squarely in the range of values reported in literature. The slight discrepancies with the results of Camacho and Ortiz may be due to differences in the treatment of the rate-dependent plasticity model and due to the comparatively coarser mesh in the present case near the impact surface due to the use of a uniform Cartesian mesh. At the moment of impact, extreme stress and velocity gradients are developed in the rod and capturing these features may require a very fine mesh. Camacho et al. used a moving finite element mesh with mesh clustering in the high-gradient regions. In future extensions of the present work, adaptive local refinement techniques will be implemented in the current Cartesian grid framework to better resolve such transient features.

The evolution of velocity magnitudes along with velocity vectors are shown in Figs. 9(a)–(d) for four different instants after impact. Initially, the base of the rod expands out rapidly, forming the foot-like shape. After around 40 μs, the base hardens and remains practically stationary, and the remaining kinetic energy is dissipated in the work required to form the second bulge, above the foot of the rod. At 80 μs, the copper rod is nearly at rest.

Table 1
Comparison of results for Taylor bar impact problem

Case	Final length (mm)	Final mushroom radius (mm)	Maximum equivalent plastic strain
Current	21.15	7.15	2.86
Camacho	Ortiz	21.42–21.44	7.21–7.24
2.97–3.25	DYNA2D	21.47	7.13
3.05	Zhu	Cescotto	21.26–21.40

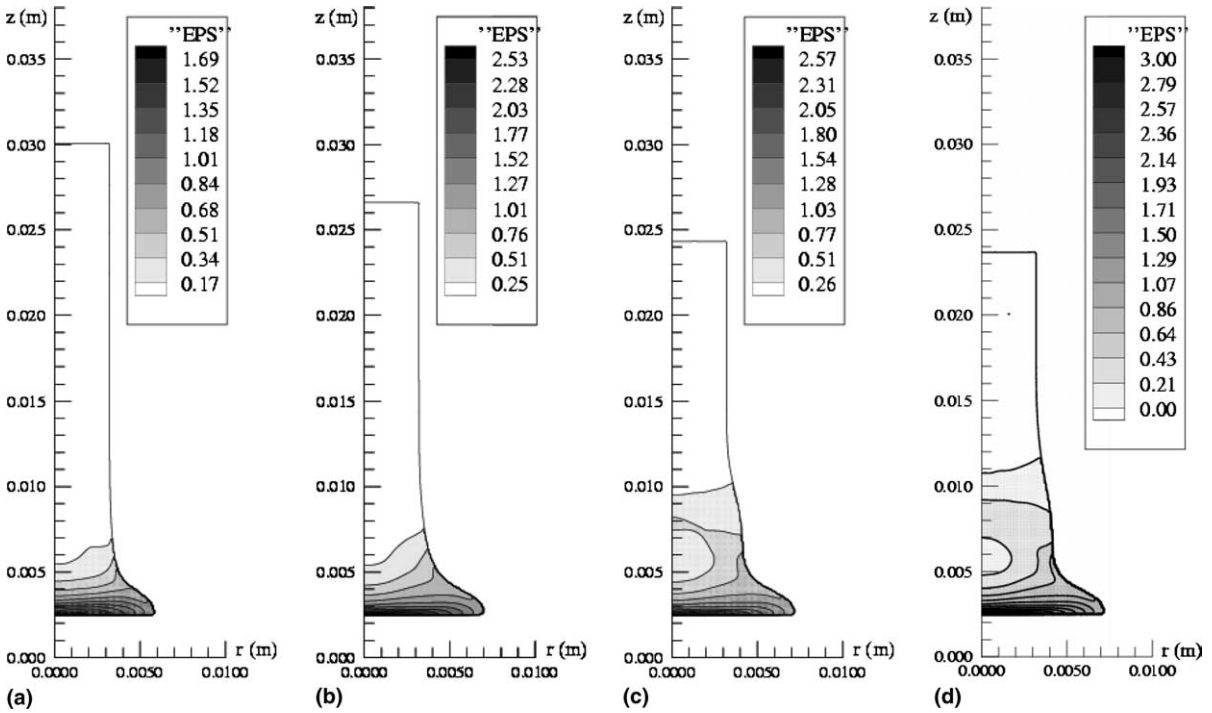

Fig. 9. Equivalent plastic strain contour at different times using 80×400 mesh. (a) 20 μs, (b) 40 μs, (c) 60 μs, and (d) 80 μs, with a velocity of 227 m/s.

Figs. 10(a)–(d) show the equivalent plastic strain contours at four different times, 20, 40, 60, and 80 μs. One can see the development of large plastic strains in the foot region and a local minimum in the plastic strain field at the symmetry axis, centered between 3 and 4 mm above the rigid surface at the symmetry axis. A large region of the rod registers negligible plastic strain. These features are clearly shown in Fig. 10(d). The values and distribution of the plastic strain are in very good agreement with the results of Camacho and Ortiz [7].

The maximum temperature of around 500 K is achieved close to the base at around the 40 μs instant, i.e., when the plastic deformation of the base reaches a maximum, as expected. This is the point in time where nearly all the plastic work done in deforming the foot has been converted to heat and raises the temperature of the foot. As the base of the foot hardens, the maximum rate of plastic work conversion moves up to form the second bulge and the heat is dissipated at that location. However, as seen from Fig. 10 the plastic strain accumulated at the second bulge is relatively small.

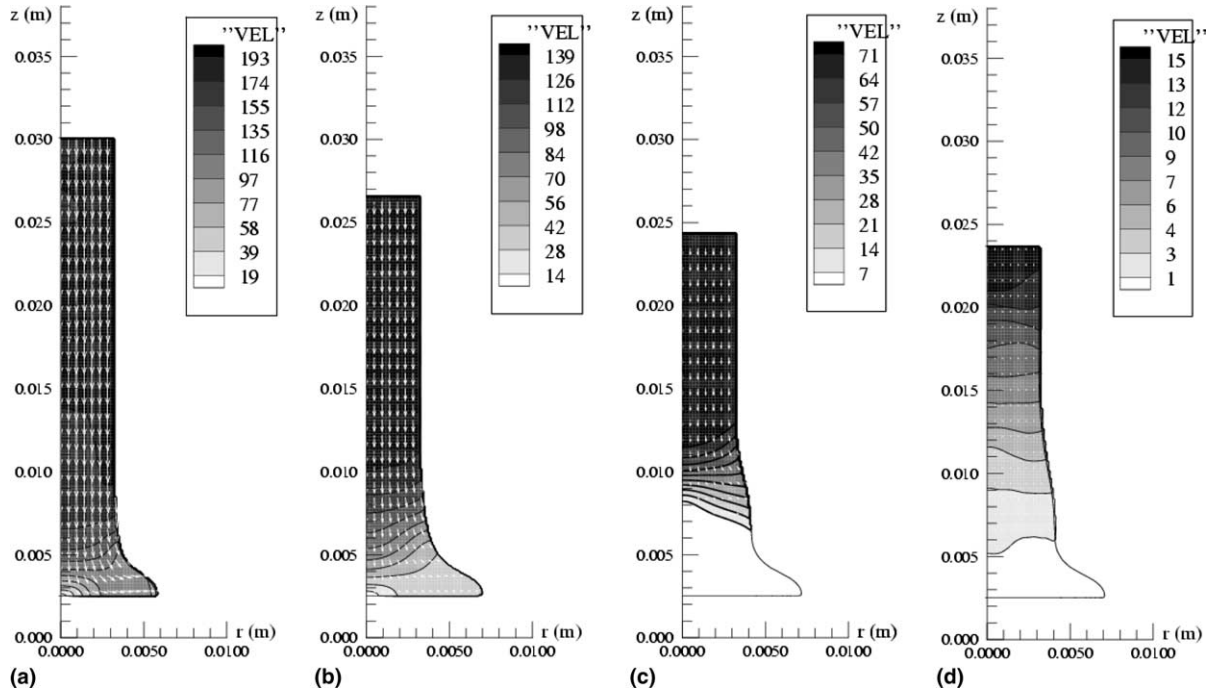

Fig. 10. Velocity magnitude contour along with velocity vector at different times using 80×400 mesh. (a) 20 μs, (b) 40 μs, (c) 60 μs, and (d) 80 μs, with a velocity of 227 m/s.

5.2. Two-dimensional axisymmetric penetration of steel target by WHA long rod

The validation of our method for two deformable objects with different material properties (a case requiring two different level sets) is carried out using a slender tungsten heavy alloy (WHA) rod projectile penetrating an initially planar target made of a steel plate with a velocity of 1250 m/s. A schematic defining the problem is shown in Fig. 11. Table 2 shows the material properties used for WHA and steel. A Johnson–Cook material model is used and the corresponding strength parameters for both materials are shown in Table 3. Note that friction between the two impacting surfaces is neglected in these calculations.

Due to the use of the uniform Cartesian grid, in order to place sufficient mesh points to resolve the tungsten rod, a very large mesh size is required. This is due to the large aspect ratio of the rod (length/radius = 25). Thus, improving the resolution in the radial direction necessitates the use of fine meshes in the vertical direction also. This limitation can be overcome by use of adaptive meshes or rectangular Cartesian meshes. However, if the latter is used, issues concerning inaccuracies in capturing large gradients oriented arbitrarily with respect to a stretched mesh will need to be addressed. We leave these aspects to future work. To enable reasonable computational effort, we limit the axial dimension of the problem to $r = 0.0125$ and study what effects this smaller domain has on the solutions.

A grid independence study is carried out using three meshes: 50×344, 75×516, and 100×688. The final shapes (at 80 μs) of the two deformed bodies are shown in Figs. 12(a)–(c). It is seen that as the grid is refined the penetration depth as well as the length of the upwelling WHA material (hereafter called ejecta) become larger. At the finest mesh, 100×688, the solution was found to be nearly grid-independent. Based on the observed trends, further refinement of the mesh will result in somewhat larger extents of the ejecta of the

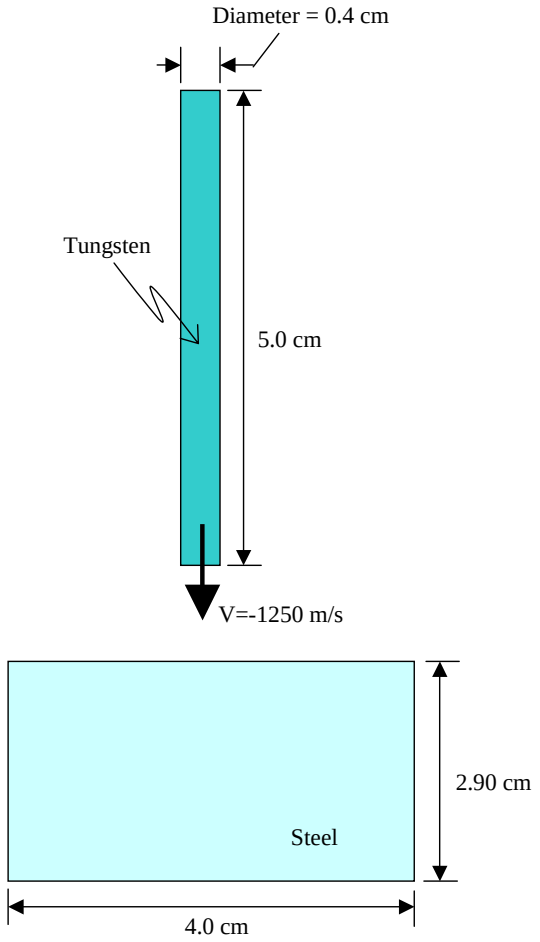

Fig. 11. Schematic of a tungsten rod penetrating a steel plate target.

Table 2
Material properties and Mie–Grüneisen equation of state parameters

Material	ρ (kg/m^3)	E (GPa)	ν	c (W/m/K)	k (J/kg/K)	Γ	c_0 (m/s)	T_m (K)
Tungsten heavy alloy	17600	200	0.29	477	38	1.43	4030	1777
High-strength steel	7850	323	0.30	134	75	1.16	4570	1723
Copper	8930	117	0.35	383.5	401	2.0	3940	1358

WHA material. For now, we will use the 100×688 mesh results, which suffice to compare the penetration rate and depth results with available experimental and numerical results [8,53].

Fig. 12(c) shows the final shape of the two deformed bodies at 80 μs for the 100×688 mesh. In Fig. 12(c), we see that the right side of the steel plate, top and bottom, barely moves from the original position. In reality the plate used in experiment has a larger radius than that shown in Fig. 12. We, therefore, examined whether the solutions obtained from our calculations on the truncated domain is valid by extending the

Table 3
Constitutive parameters

Material	Y_0 (GPa)	B (GPa)	N	C	m	G (GPa)
Tungsten heavy allow	1.51	0.177	0.12	0.016	1.00	124.0
High-hard steel	1.50	0.569	0.22	0.003	1.17	77.3
Copper	0.400	0.100	1.0	0.025	1.09	43.33

$\sigma_y = (Y_0 + B\bar{\varepsilon}_p^n)\left[1 + C\ln(\dot{\bar{\varepsilon}}_p/\dot{\varepsilon}_0)\right](1-\theta^{*m})$, $\dot{\varepsilon}_0 = 1.0\ \mathrm{s}^{-1}$, $\theta^* = \frac{T-T_0}{T_m-T_0}$, $T_0 = 294$ K.

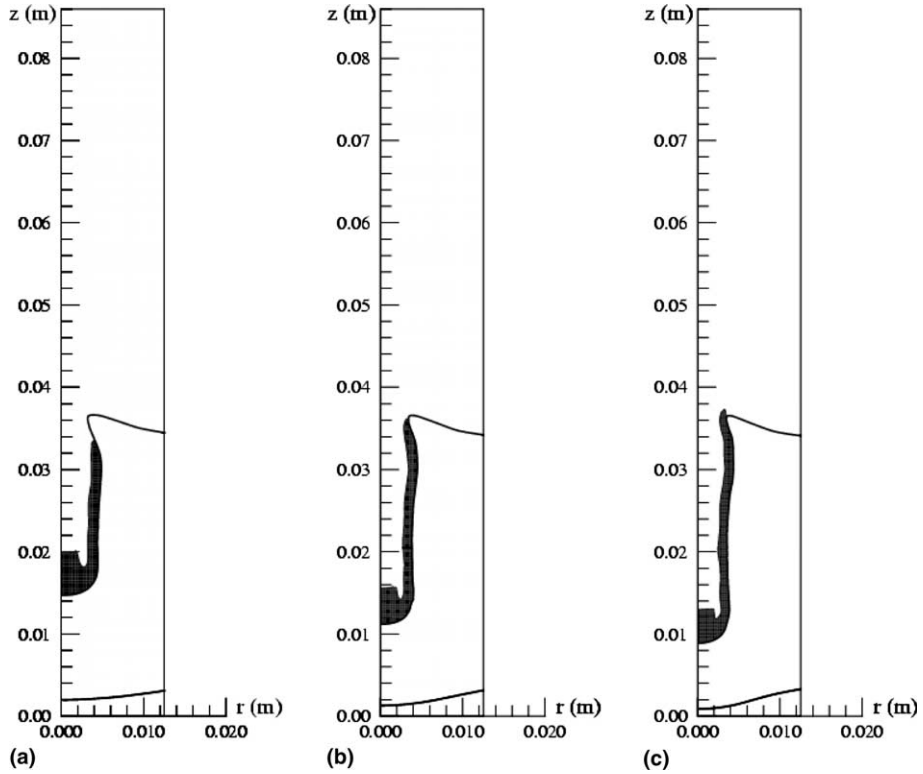

Fig. 12. Grid refinement study of a tungsten rod penetrating a steel plate with a velocity of 1250 m/s. (a) 50×344 mesh, (b) 75×516 mesh, and (c) 100×688 mesh.

width of steel plate from 0.0125 to 0.02 m, while maintaining the same grid density as the 100×688 mesh. This extended domain case for the steel plate ($r = 0.02$ m) is shown in Figs. 13(a)–(d) with evolution of the two deformed bodies at times of 20, 40, 60, and 80 μs for a mesh of 160×688 points. Note that, due to the large aspect ratio of the problem, even for this fairly large mesh size, there are only 16 mesh points within the initial rod radius. Nevertheless, the results obtained agree very well with the benchmarks and with experiments as demonstrated below. The top and bottom surfaces of the steel plate do not deform much at $r \geqslant 0.01$ m. This behavior agrees well with calculations reported by Camacho and Ortiz. The ejected length of WHA material (Fig. 13(d)) is slightly shorter compared to that for narrower domain ($r = 0.0125$ m) in Fig. 12(c). This is perhaps due to the absorption and dissipation of energy within the larger mass of material in the plate in the extended domain case. In particular, the top surface of the steel plate appears to deform more for the extended domain case shown in Fig. 12(c). However, the main features of the computed

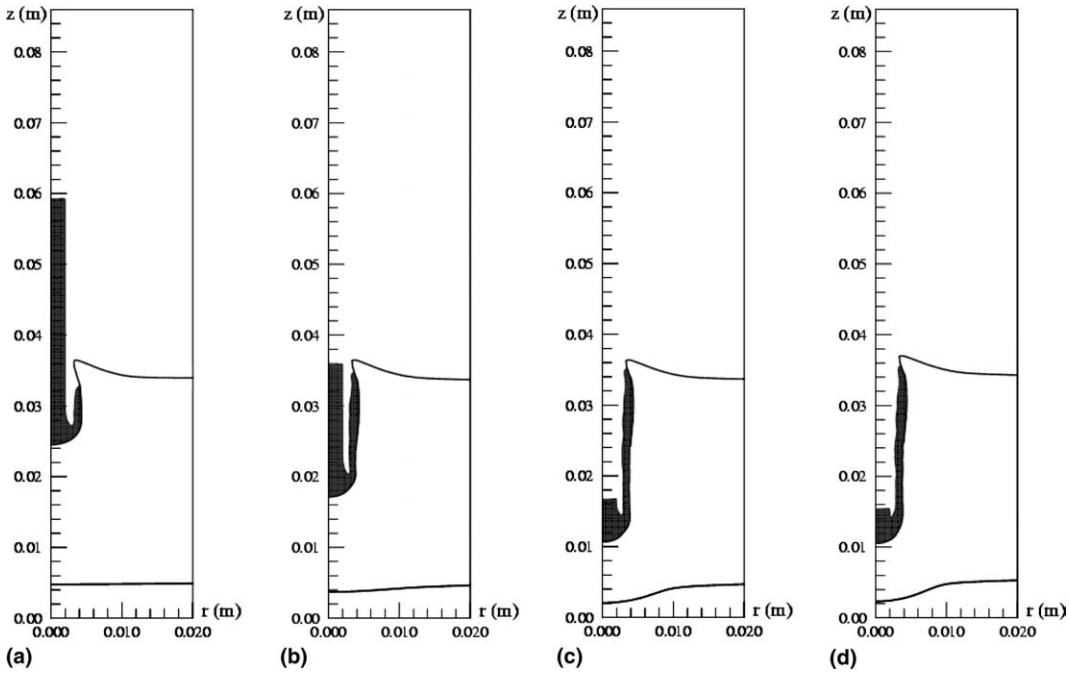

Fig. 13. Shapes of a tungsten rod penetrating a steel plate using 160×688 mesh, with a velocity of 1250 m/s. (a) 20 μs, (b) 40 μs, (c) 60 μs, and (d) 80 μs.

solutions appear to be relatively insensitive to the domain size and thus the truncation of the domain to facilitate computational economy does not appear to be very significant.

The evolution of equivalent plastic strain is shown in Figs. 14(a)–(d) for the extended domain with a 160×688 mesh. The maximum equivalent plastic strain is found to be around 4.5, occurring mostly near the impact surfaces. The values of equivalent plastic strain are higher in the WHA material compared to those in the steel material. The plastic strains obtained by Camacho and Ortiz using Lagrangian finite element method with an adaptive mesh agree very well with the present results, both in terms of the magnitude and distributions of the plastic strains. In particular, a trough in the plastic strain distribution is noticed in both our results as well as those of Camacho and Ortiz and occurs near the bottom surface in the steel plate at the symmetry axis, as seen in Fig. 14(d). The ejection length of the WHA material is higher in the Camacho and Ortiz calculations when compared to our results. However, the resolution of the ejected region afforded by the mesh used in the present calculations is too low, with just three mesh points across the vertically oriented trails of the ejecta. The grid refinement study performed above indicates that as the mesh is refined further the length of the ejecta will increase. As shown below, at the current mesh resolution, the overall penetration characteristics and material deformation are adequately predicted.

Figs. 15(a)–(d) show the v-component velocity contour at different times, 20, 40, 60, and 80 μs, for the extended domain with a 160×688 mesh. The maximum positive v-component velocity is observed around 40 μs, occurring in the ejecting mass of the WHA material. Around 80 μs, the rod comes to rest and only small residual velocities remain.

The maximum temperatures occur around the impacted surfaces as this the region of maximum rate of conversion of plastic work to heat. The recorded maximum temperature is around 1300 K in the WHA

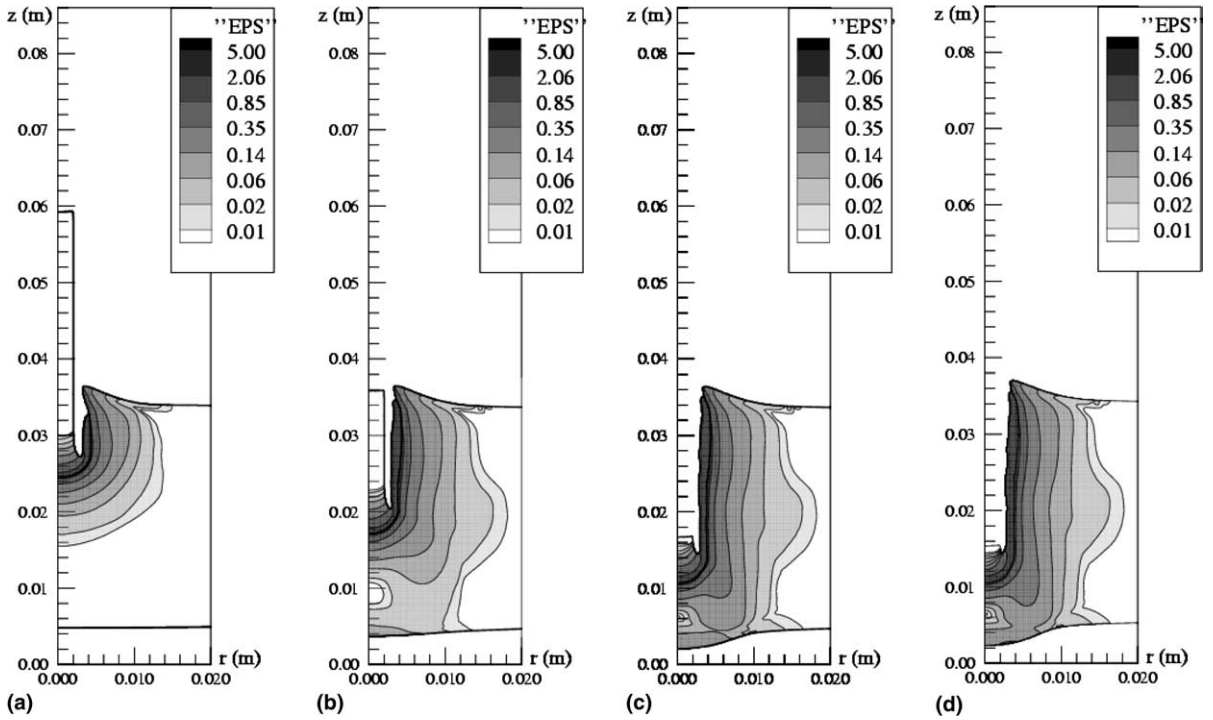

Fig. 14. Equivalent plastic strain contour of a tungsten rod penetrating a steel plate calculation using 160×688 mesh, with a velocity of 1250 m/s. (a) 20 μs, (b) 40 μs, (c) 60 μs, and (d) 80 μs.

material, below the melting temperature of 1777 K for WHA and 1723 K for steel. The largest temperature occurs at around 40 μs and decreases as the rod goes to rest state. This shows that the largest plastic work done occurs before this time of 40 μs.

Fig. 16 shows the projectile nose and tail trajectories as a function of time, for the extended domain case, and is compared with the superposed results from experiment [52] and from Camacho and Ortiz [7]. Also plotted are the original rear and impact surfaces. Our results show reasonable agreement with those of experiment and Camacho and Ortiz. The tail trajectory is in much better agreement as its surface experiences less extreme conditions during impact and penetration. The present calculation predicts the penetration depth in good agreement with experiments. Despite the marginal resolution of the ejected trails, the overall penetration and deformation behavior is predicted in good accord with the adaptive finite element simulations of Camacho and Ortiz [7].

Fig. 17 shows the projectile nose (upper curves) and tail (lower curves) velocity histories, for the extended domain case, compared against the results from experiment [52] and from Camacho and Ortiz [7]. Note that since the results from Camacho and Ortiz display considerable noise in the initial phases after impact, the plotted values were hand-picked to show only a few representative points after smoothing their curves. Similar conclusions can be drawn as in Fig. 16, the velocity data obtained from the present calculations being in good agreement with the benchmarks with the tail results being in better agreement than nose results. The oscillatory nature of the results, seen in both the present and the FEM calculations of Camacho and Ortiz, is perhaps due to the transient wave phenomena in the initial stages of impact.

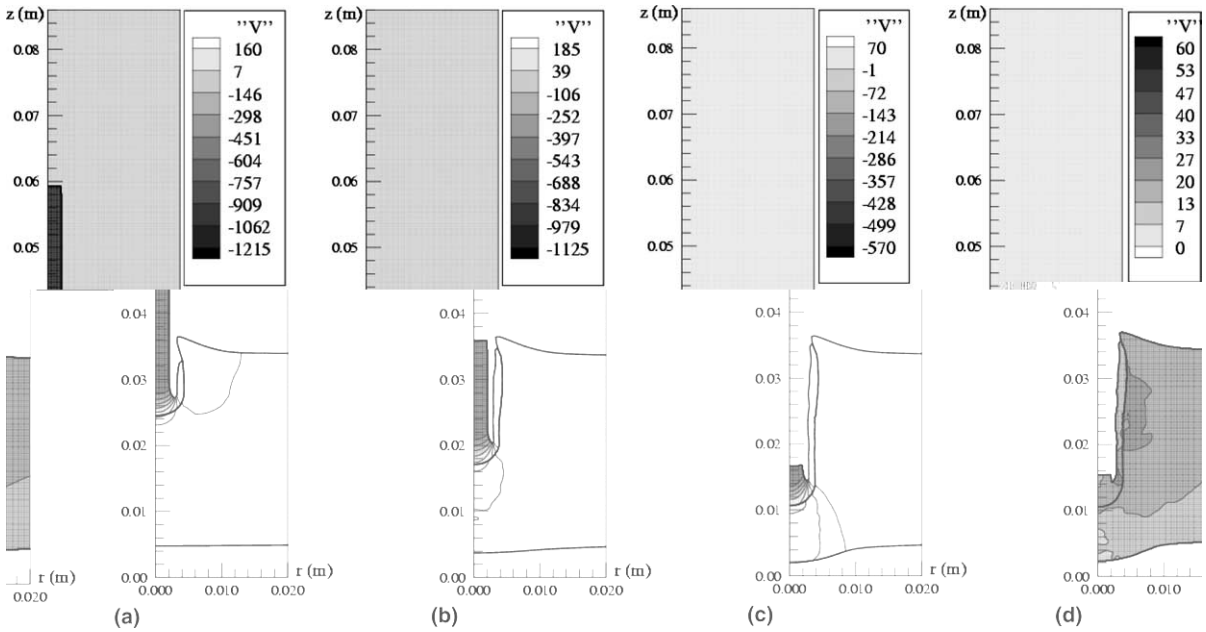

Fig. 15. v-component velocity contour of a tungsten rod penetrating a steel plate calculation using 160×688 mesh, with a velocity of 1250 m/s. (a) 20 μ s, (b) 40 μs, (c) 60 μs, and (d) 80 μs.

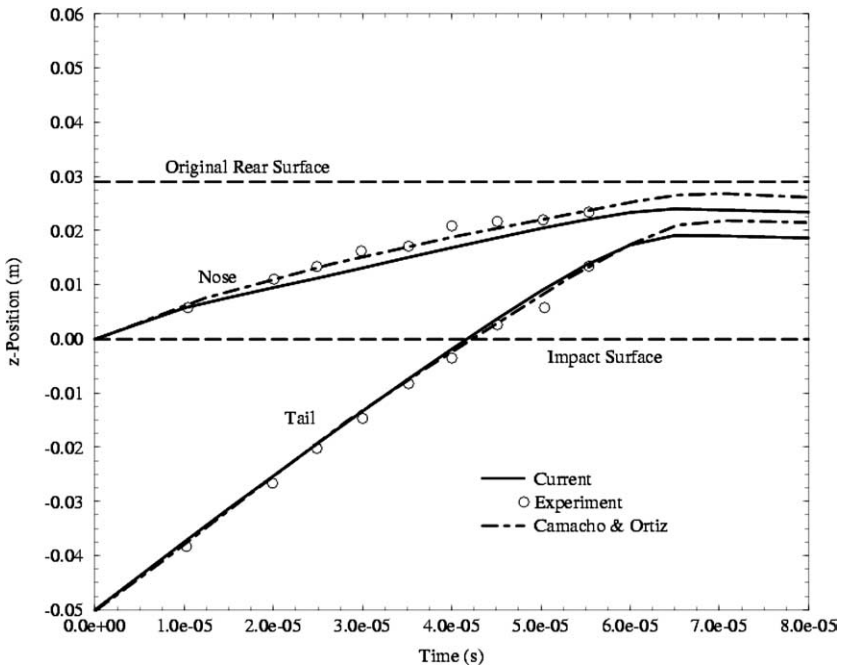

Fig. 16. Projectile nose and tail trajectories of a tungsten rod penetrating steel plate using a 160×688 mesh, with a velocity of 1250 m/s.

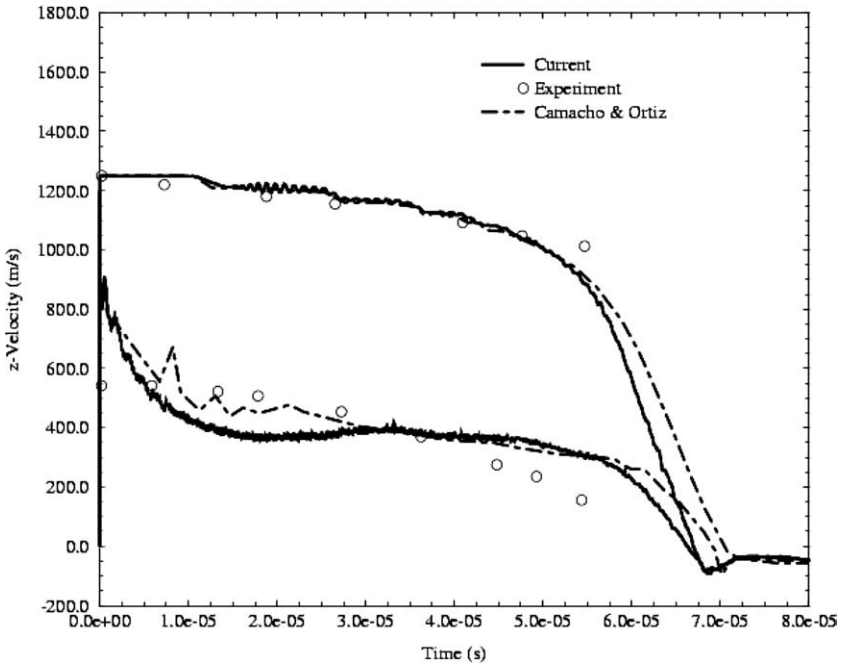

Fig. 17. Projectile nose and tail velocity histories of a tungsten rod penetrating steel plate using a 160×688 mesh, with a velocity of 1250 m/s.

5.3. Two-dimensional axisymmetric void collapse in a copper matrix

In this test case, a spherical void with a radius of 1 μm within a copper matrix undergoes axisymmetric deformation due to a propagating shock created by imposing a particle velocity at the bottom boundary (i.e., simulating a piston moving at specified speeds). A schematic of the problem is shown in Fig. 18. The impulsive velocity supplied at the bottom boundary seeks to simulate the effect of impact at the bottom surface of the copper plate. The material response is modeled using a Johnson–Cook model, with constants applicable to copper (Table 3). The wave moves through the copper matrix and is transmitted out through the upper boundary. The right boundary is subjected to symmetric conditions, whereas the left boundary is the axis of symmetry. The simulation is carried out for three different initial piston velocities: 50, 200, and 500 m/s, using a 200×400 mesh. The void collapse phenomenon has implications for the initiation process in energetic materials [21,53–55]. Here, we examine the behavior of the void in copper, for which the material parameters are well characterized. Void collapse can occur in different modes depending on the strength of the impinging shock. As the shock strength increases the void collapse goes from a nearly spherical (visco-plastic) mode to a jet (hydrodynamic) mode where the lower surface of the void forms a jet which impacts on the upper surface at high velocity. The criterion for the transition from the visco-plastic to hydrodynamic mode is provided by the analysis of Khasainov [56] in terms of the ratio of shock passage time to the void deformation time scales. When the shock passage time scale is larger than the void collapse time scale the mode of collapse is visco-plastic; when the shock passage time scale is comparable with the void collapse time scale the mode of collapse is hydrodynamic. This latter mode is characterized by the formation of a jet of material which issues from the lower side of the void and impacts the upper side, leading to large temperatures on the impact location due to dissipation of kinetic energy of the jet. This transition is displayed in the following results.

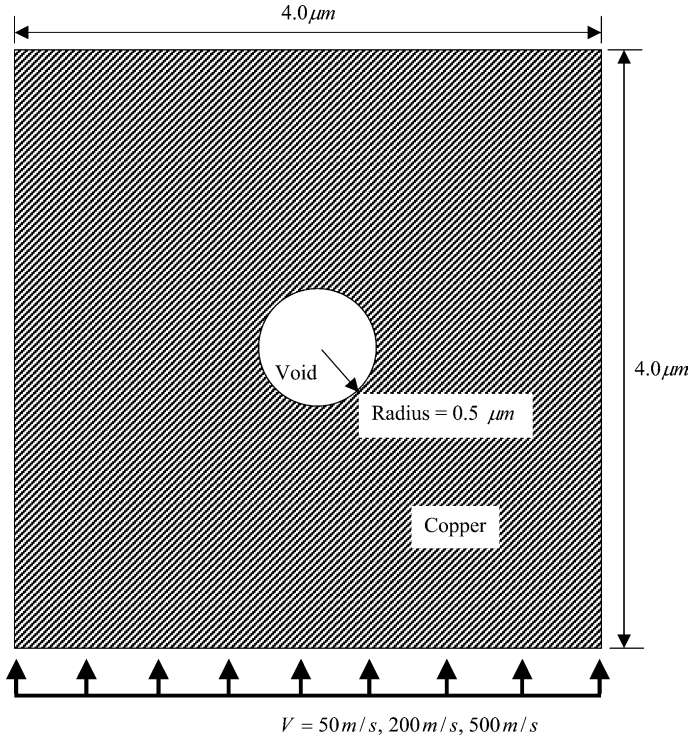

Fig. 18. Schematic of setup for void collapse in a copper matrix.

For the low impact velocity case, i.e., 50 m/s, Figs. 19(a) and (b) show the void at $t = 2.52\text{e} - 9$ s, after which further deformation nearly ceases. The figures show the final shape (Fig. 19(a)), pressure contour (Fig. 19(a)), temperature contours (Fig. 19(b)), and velocity magnitude contour (Fig. 19(b)) along with streamlines. The maximum temperature achieved is around 404 K, occurring around the void. The collapsing process is not concentric as the original void center was at $(0, 2\text{e} - 06)$ m. However, the void does not markedly deviate from its original spherical shape. No jetting phenomenon is observed, although the maximum v-component velocity ($\sim$100 m/s) is at the lower surface at the axisymmetric coordinate. The kinetic energy developed due to the imposed shock is dissipated through plastic work. Fig. 20 shows the evolution of shapes of the void at equal time intervals. Most of the deformation occurs on the lower surface, and during the earlier phase of the process.

Results for imposed boundary velocity of 200 m/s, i.e., intermediate shock strength, are shown in Figs. 21(a) and (b) at $t = 9.45\text{e} - 10$ s. This void collapses completely and the instant shown is shortly before complete void collapse. The figures show the final shape (Fig. 21(a)), pressure contour (Fig. 21(a)), temperature contour (Fig. 21(b)), and velocity magnitude contour (Fig. 21(b)) along with streamlines. It is observed that in this case, jetting occurs to some extent, with maximum jetting velocity around 2600 m/s. The maximum temperature in the material during the collapse is around 1570 K, which is above the melting temperature of 1400 K for copper. The highest temperatures occur around the collapsing void as this is where highest rate of plastic work is localized.

Fig. 22 shows the evolution of the shapes during the void collapse process plotted at equal time intervals. The jetting phenomenon is clearly observed, eventually breaking the void at the symmetry axis into two

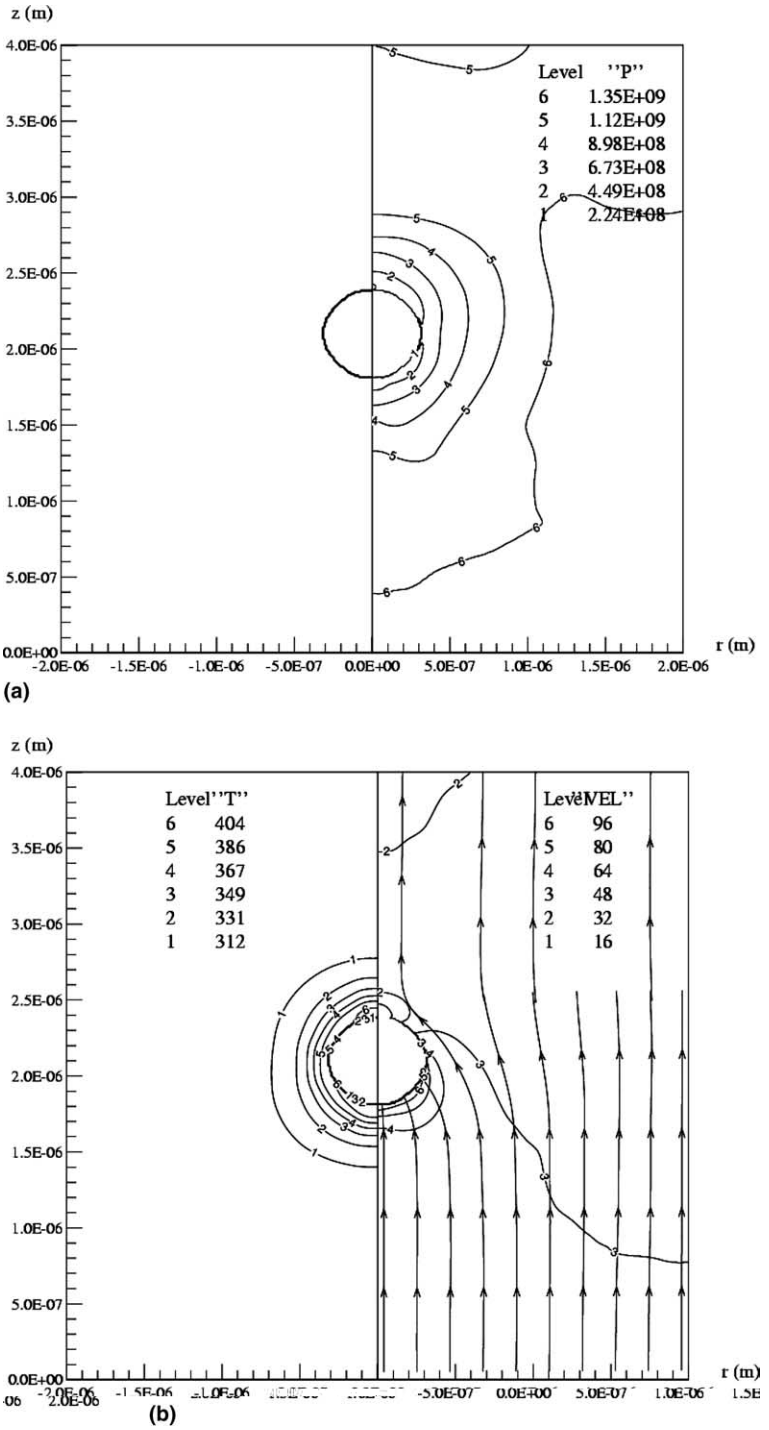

Fig. 19. Void collapse calculation using 200×400 mesh in a copper matrix, with a diameter $= 1$ μm, $V = 50$ m/s, and $t = 2.52 \times 10^{-9}$ s. (a) left – shape, right – pressure contour, (b) left – temperature contour, right – velocity magnitude contour and velocity streamline.

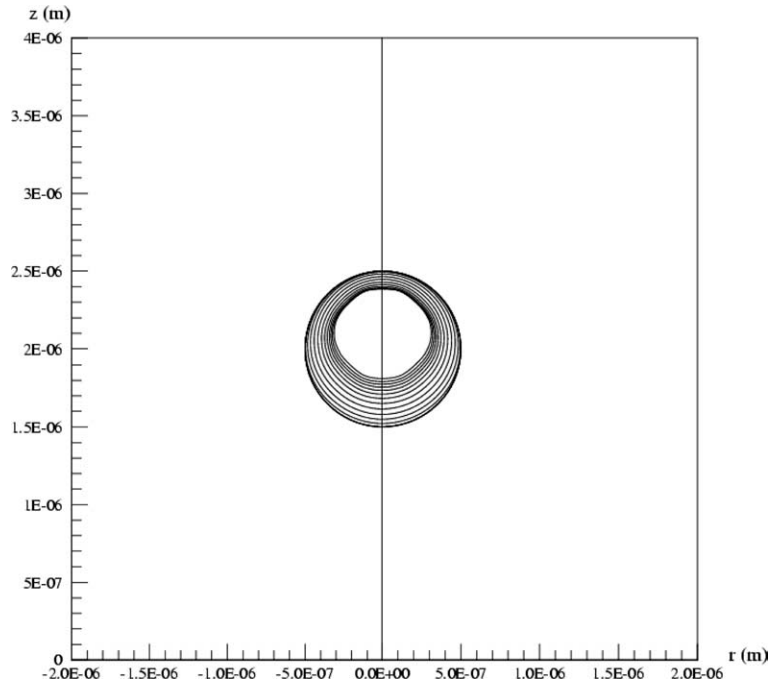

Fig. 20. Shapes at different times of void collapse process using 200×400 mesh in a copper matrix, with a diameter $= 1$ μm and $V = 50$ m/s.

smaller voids, which eventually disappear. This simulation demonstrates the ability of the method to handle extreme topological changes.

For an imposed particle velocity of 500 m/s, i.e., the highest shock strength, the flow field at three different times during the collapse process, i.e., 3.78×10^{-10}, 5.67×10^{-10}, and 6.93×10^{-10} s, are shown in Figs. 23–25. Final shapes (a), pressure contour (a), temperature contour (b), and velocity magnitude contours (b) along with streamlines are plotted in each figure. For this high strength of shock, a distinct jet can be observed, with the highest velocity of the jetting material being around 4130 m/s, much higher than the imposed particle velocity, and the maximum temperature recorded during the collapse process is around 2110 K, well above the melting temperature of copper. One can see that the void would be completely collapsed before the shock wave reaches the top boundary of the domain, i.e., the shock passage time in this case is comparable with the void collapse time. This case represents the hydrodynamic mode of collapse in agreement with the criterion mentioned above. The maximum temperatures are concentrated around the void, and increase from 426 K (at 3.78×10^{-10} s) to 2110 K (at 6.93×10^{-10} s), as the plastic work is dissipated as heat.

Fig. 26 shows the evolution of the void collapse process. One can see a clear jetting phenomenon after the time of 5.67×10^{-10} s. Following the final shape shown, the void is completely collapsed and thus the void space disappears. The computational method is capable of simulating the entire process of void deformation, collapse, and disappearance.

6. Conclusions

We have developed a numerical technique designed to solve problems involving high-speed multimaterial interactions occurring in impact, penetration and collapse. The distinguishing feature of the approach

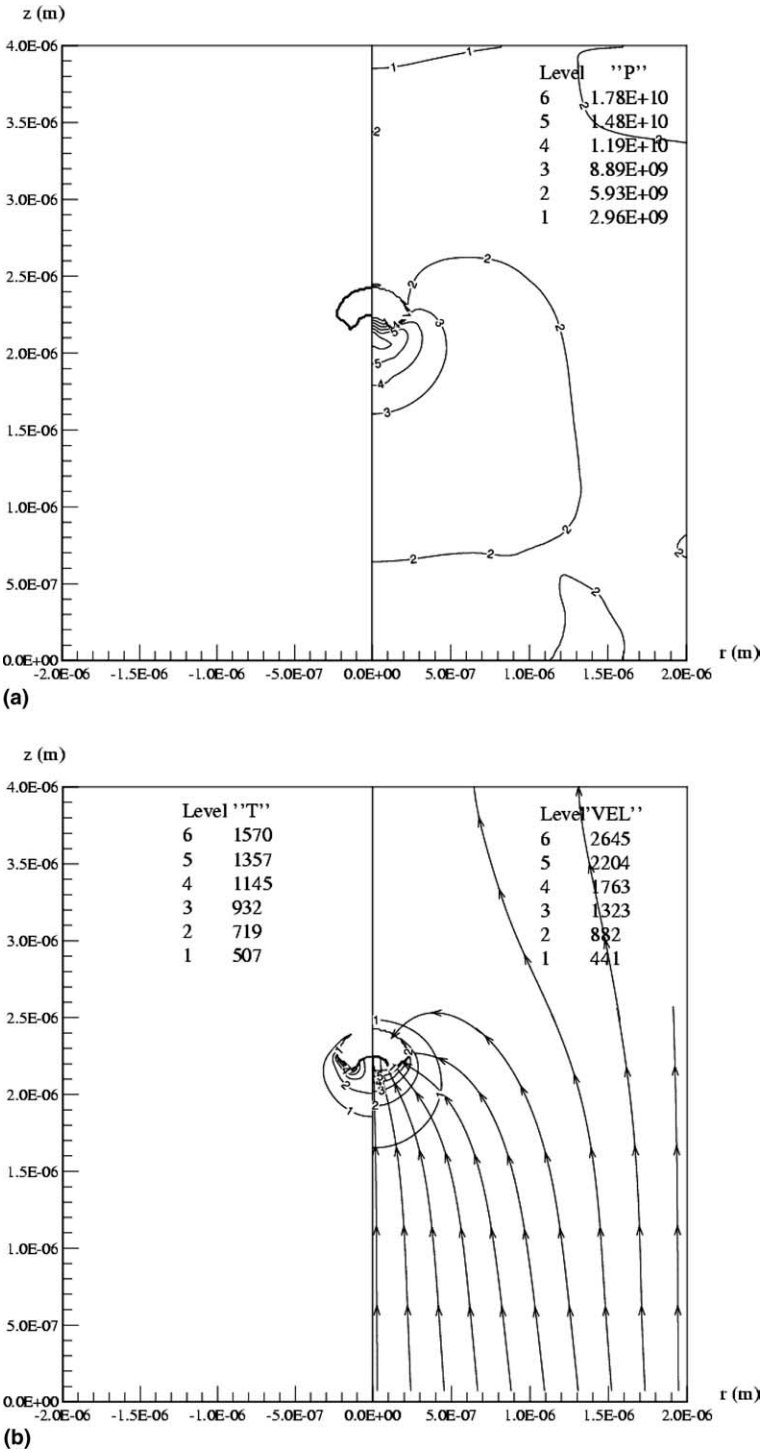

Fig. 21. Void collapse calculation using 200×400 mesh in a copper matrix, with a diameter $= 1$ μm, $V = 200$ m/s, and $t = 9.45 \times 10^{-10}$ s. (a) left – shape, right – pressure contour, (b) left – temperature contour, right – velocity magnitude contour and velocity streamline.

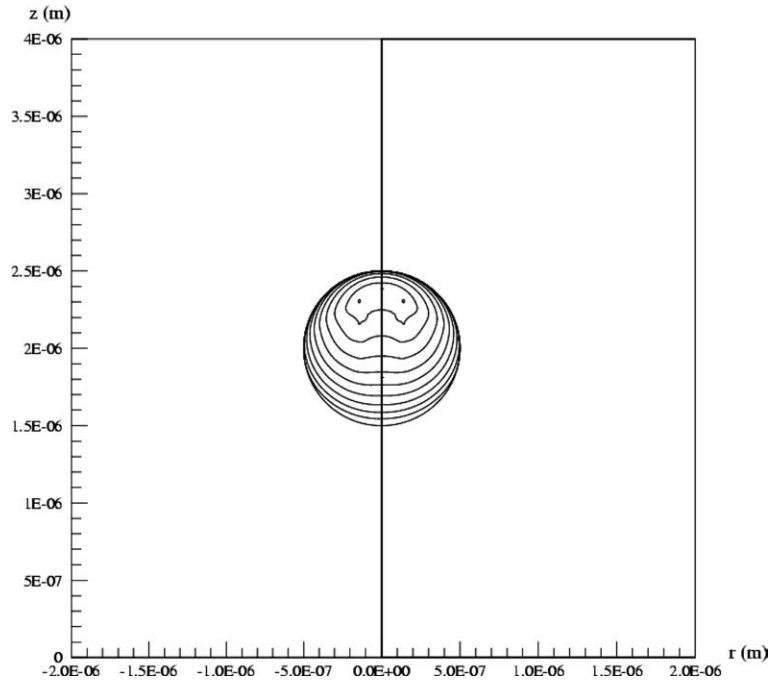

Fig. 22. Shapes at different times of void collapse process using 200×400 mesh in a copper matrix, with a diameter $= 1$ μm and $V = 200$ m/s.

presented here is that the shortcomings associated with traditional Eulerian and Lagrangian methods are avoided. The methodology can easily be extended to three-dimensions. The technique can handle the following physical phenomena typical of impact problems:

1. Large deformations, including fragmentation and merger of the materials. All boundaries are treated in a sharp manner. The grid remains fixed however and problems associated with maintaining a high-quality grid under large deformations do not arise.
2. Nonlinear wave-propagation and the development of shocks in materials governed by rate-dependent plasticity. The nonlinear waves are tracked using high-resolution shock capturing schemes implemented on the fixed grid.
3. Accurate elasto-plastic behavior of the material during impact. This aspect is captured for material response governed by the Johnson–Cook model and a radial return algorithm to maintain consistency with the yield surface.

For two-dimensional problems, the hybrid particle level set method is used to track boundaries with sharp corners that are carried without deterioration through the large deformations of the materials. Benchmark calculations for the multi-dimensional case including axisymmetric Taylor bar impact and penetration of a Tungsten rod into steel plate show excellent agreement with moving finite element solutions. Qualitative agreement with theory is shown for void collapsing process in an impacted material containing a spherical void. The method has thus been shown to be suitable for applications involving high-velocity, multimaterial impacts leading to large strain-rates, nonlinear elasto-plastic waves, and topological changes.

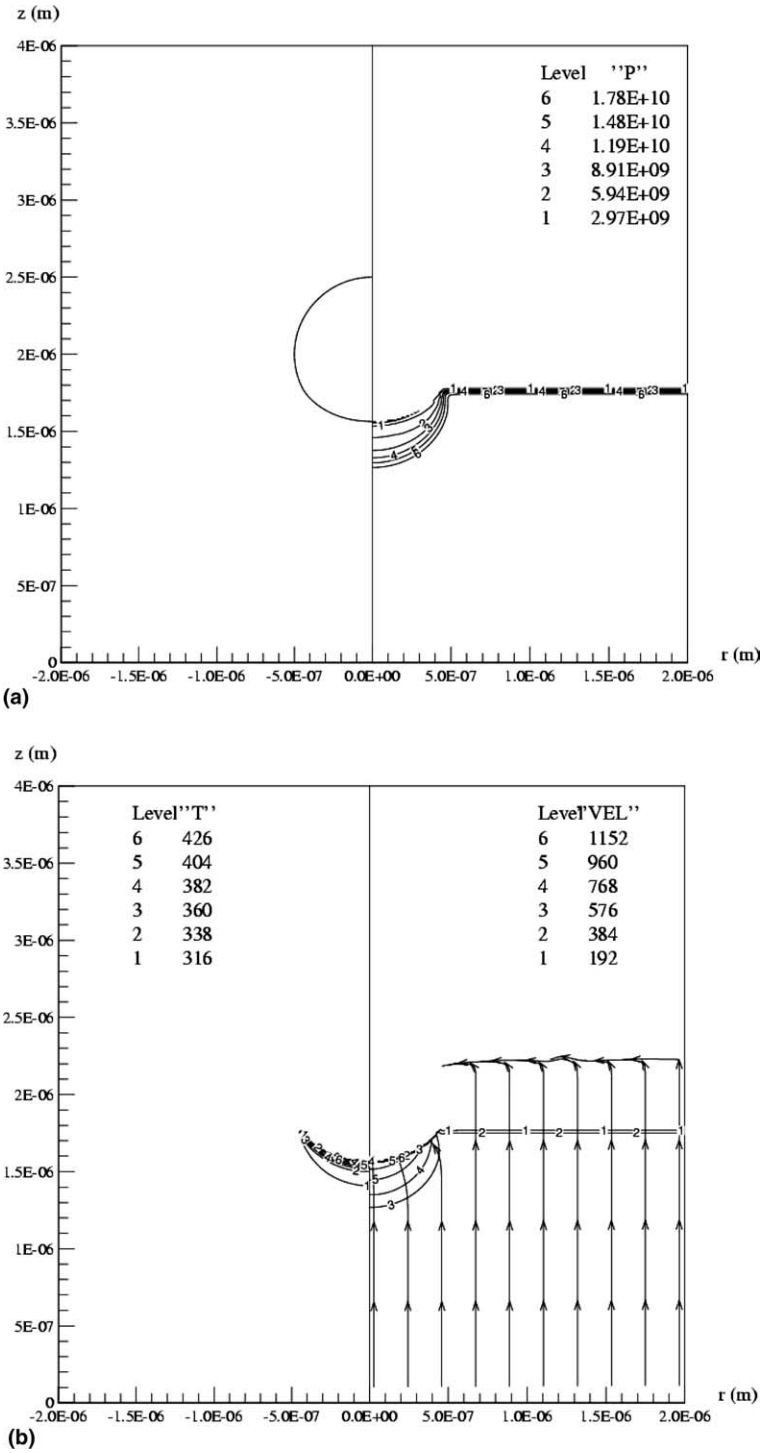

Fig. 23. Void collapse calculation using 200×400 mesh in a copper matrix, with a diameter $= 1$ μm, $V = 500$ m/s, and t $= 3.78 \times 10^{-10}$ s. (a) left – shape, right – pressure contour, (b) left – temperature contour, right – velocity magnitude contour and velocity streamline.

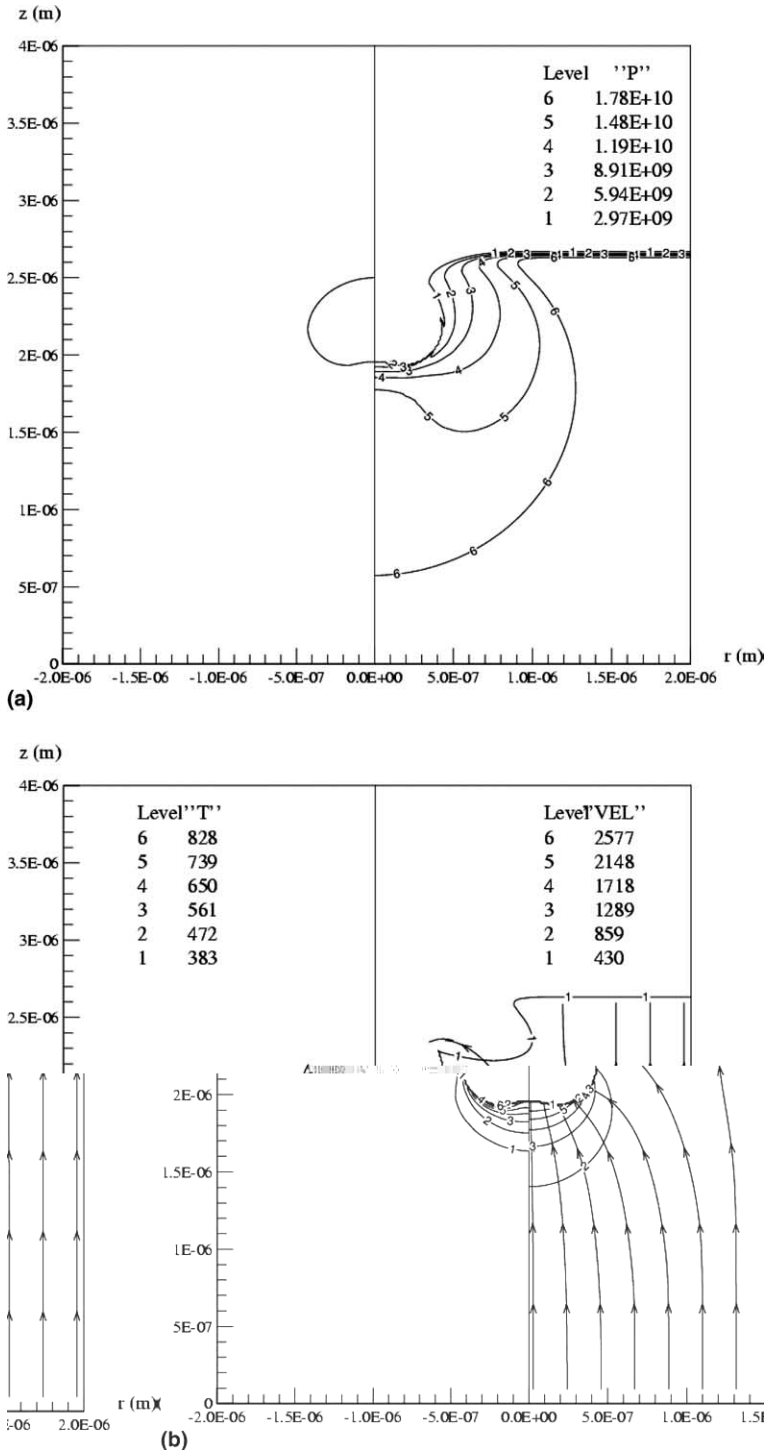

Fig. 24. Void collapse calculation using 200×400 mesh in a copper matrix, with a diameter = 1 μm, $V = 500$ m/s, and $t = 5.67 \times 10^{-10}$ s. (a) left – shape, right – pressure contour, (b) left – temperature contour, right – velocity magnitude contour and velocity streamline.

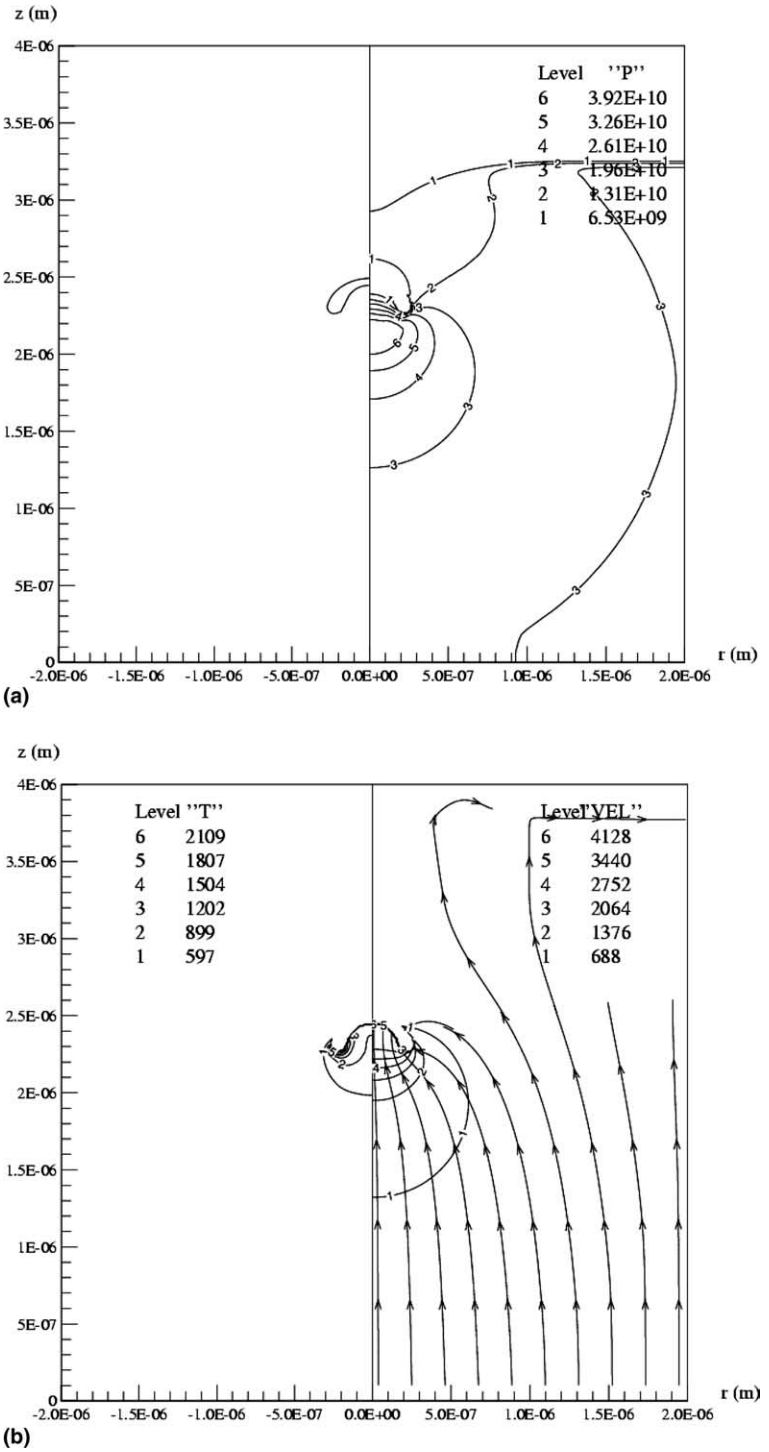

Fig. 25. Void collapse calculation using 200×400 mesh in a copper matrix, with a diameter $= 1$ μm, $V = 500$ m/s, and $t = 6.93 \times 10^{-10}$ s. (a) left – shape, right – pressure contour, (b) left – temperature contour, right – velocity magnitude contour and velocity streamline.

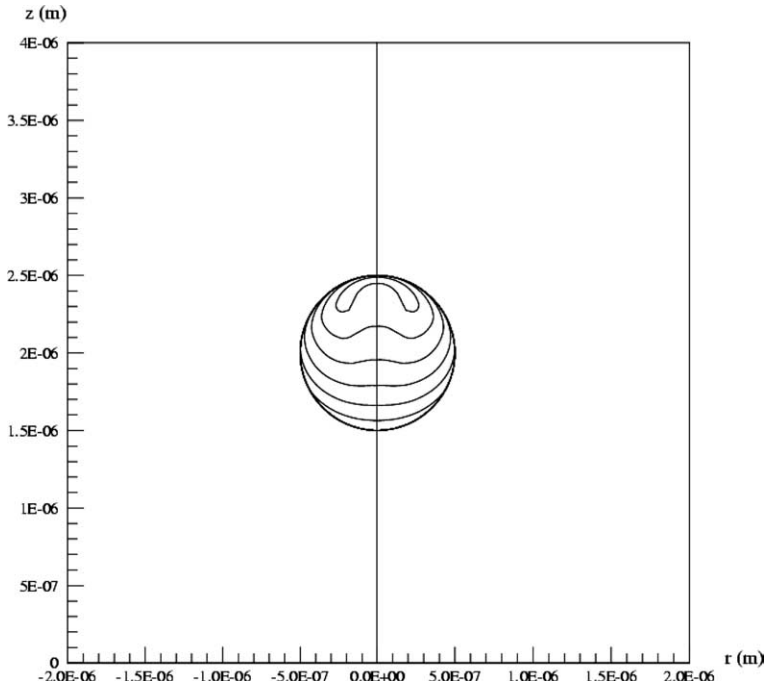

Fig. 26. Shapes at different times of void collapse process using 200×400 mesh in a copper matrix, with a diameter $= 1$ μm and $V = 500$ m/s.

Acknowledgements

This work was supported by a grant from Air Force Research Lab, Eglin AFB, FL (Project manager Dr. K.J. Vanden) and AFOSR Computational Mathematics Program (Project manager Major W. Hilbun). Discussions with Prof. Jia Lu (Department of mechanical and industrial engineering, U Iowa) on aspects of plasticity are gratefully acknowledged.

References

[1] J.A. Zukas, T. Nicholas, H.F. Swift, L.B. Gresczuk, D.R. Curran, Impact Dynamics, Wiley, New York, 1982.
[2] M.A. Meyers, Dynamic Behavior of Materials, John Wiley & Sons, New York, 1994.
[3] C.E. Anderson Jr., S.R. Bodher, Ballistic impact: the status of analytical and numerical modeling, Int. J. Impact Eng. 7 (1988) 9–35.
[4] D.J. Benson, Computational methods in Lagrangian and Eulerian hydrocodes, Comput. Methods Appl. Mech. Engrg. 99 (1992) 235–395.
[5] W.-K. Liu, T. Belytschko, H. Chang, An arbitrary Lagrangian–Eulerian finite element method for path-dependent materials, Comput. Methods Appl. Mech. Engrg. 58 (1986) 227–245.
[6] G.T. Camacho, M. Ortiz, Computational modeling of impact damage in brittle materials, Int. J. Solids Struct. 33 (1996) 2899–2938.
[7] G.T. Camacho, M. Ortiz, Adaptive Lagrangian modeling of ballistic penetration of metallic targets, Comput. Methods Appl. Mech. Engrg. 142 (1997) 269–301.
[8] A. Duarte, J.T. Oden, An h–p adaptive method using clouds, Comput. Methods Appl. Mech. Engrg. 139 (1996) 237–262.
[9] G.R. Johnson, R.A. Stryk, S.R. Beissel, SPH for high velocity impact computations, Comput. Methods Appl. Mech. Engrg. 139 (1996) 347–373.

[10] W.-K. Liu, S. Hao, T. Belytschko, S. Li, C.T. Chang, Multi-scale methods, Int. J. Numer. Methods Engrg. 47 (7) (2000).
[11] T. Belytschko, Y. Guo, W.-K. Liu, S.P. Xiao, Unified stability analysis of meshless particle methods, Int. J. Numer. Methods Engrg. 48 (9) (2000).
[12] J. Dolbow, John, N. Moes, T. Belytschko, Discontinuous enrichment in finite elements with a partition of unity method, Finite Elements Anal. Des. 36 (3) (2000).
[13] N. Moes, J. Dolbow, T. Belytschko, Finite element method for crack growth without remeshing, Int. J. Numer. Methods Engrg. 46 (1) (1999) 131–150.
[14] N. Sukumar, N. Moes, B. Moran, T. Belytschko, Extended finite element method for three-dimensional crack modelling, Int. J. Numer. Methods Engrg. 48 (2000) 1549–1570.
[15] J.A. Trangenstein, A second-order algorithm for the dynamic response of soils, Impact Comput. Sci. Engrg. 2 (1990) 1–39.
[16] J.A. Trangenstein, A second-order algorithm for two-dimensional solid mechanics, Comput. Mech. 13 (1994) 343–359.
[17] J.A. Trangenstein, Adaptive mesh refinement for wave propagation in nonlinear solids, SIAM J. Sci. Comput. 16 (1995) 819–939.
[18] J.A. Trangenstein, R.B. Pember, The Riemann problem for longitudinal motion in an elastic–plastic bar, SIAM J. Sci. Stat. Comput. 12 (1991) 180–207.
[19] D.J. Benson, A multi-material Eulerian formulation for the efficient solution of impact and penetration problems, Comput. Mech. 15 (1995) 558–571.
[20] S.R. Cooper, D.J. Benson, V.F. Nesterenko, A numerical exploration of the role of void geometry on void collapse and hot spot formation in ductile materials, Int. J. Plasticity 16 (2000) 525–540.
[21] R. Menikoff, E. Kober, Compaction waves in granular HMX, Los Alamos National Lab Report, LA-13456-MS, 1999.
[22] P. Glaister, An approximate Riemann solver for the Euler equations for real gases, J. Comput. Phys. 74 (1988) 382–408.
[23] M. Arienti, E. Morano, J. Shepherd, Nonreactive Euler flows with Mie–Grüneisen equation of state for high explosives. Available from: http://www.caltech.edu/~eric/Papers/FM99-8.pdf, 1999.
[24] J.K. Dukowicz, A general, non-iterative Riemann solver for Godunov's method, J. Comput. Phys. 61 (1985) 119–137.
[25] G. Miller, E. Puckett, A high-order Godunov method for multiple condensed phases, J. Comput. Phys. 128 (1996) 134–164.
[26] R.P. Fedkiw, T. Aslam, B. Merriman, S. Osher, A non-oscillatory Eulerian approach to interfaces in multimaterial flows (The Ghost Fluid Method), J. Comput. Phys. 152 (1999) 457–492.
[27] H.S. Udaykumar, L. Tran, D.M. Belk, K.J. Vanden, An Eulerian method for computation of multimaterial impact with ENO-shock capturing and sharp interfaces, J. Comput. Phys. 186 (2003) 136–177.
[28] D. Enright, R. Fedkiw, J. Ferziger, I. Mitchell, A hybrid particle level set method for improved interface capturing, J. Comput. Phys. 176 (2002) 205–227.
[29] G.I. Taylor, H. Quinney, The latent energy remaining in a metal after cold working, Proc. R. Soc., Ser. A 143 (1934) 307–326.
[30] G.R. Johnson, W.H. Cook, Fracture characteristics of three metals subjected to various strains, strain rates, temperatures and pressures, Eng. Fract. Mech. 21 (1) (1985) 31–48.
[31] K.J. Vanden, Characteristic analysis of the uniaxial stress and strain governing equations with thermal–elastic and Mie–Gruneison equation of state, Technical Memorandum, AFRL, Eglin AFB, Eglin, FL, 1998.
[32] C.-W. Shu, S. Osher, Efficient implementation of essentially non-oscillatory shock-capturing schemes, J. Comput. Phys. 77 (1988) 439–471.
[33] C.-W. Shu, S. Osher, Efficient implementation of essentially non-oscillatory shock-capturing schemes II, J. Comput. Phys. 83 (1989) 32–78.
[34] B. Olinger, P.M. Halleck, H.H. Cady, The isothermal linear volume compression of PETN to 10 GPa and the calculated shock compression, J. Chem. Phys. 62 (1975) 4480–4483.
[35] F.J. Montáns, R.I. Borja, Implicit J_2 -bounding surface plasticity using Prager's translation rule, Int. J. Numer. Methods Engrg. 55 (2002) 1129–1166.
[36] A. Bilotta, Integration of constitutive equations for 2D elasto-plastic bodies, Manuscript available from: http://www.labmec.unical.it/libreria/download/report_23.pdf, 2001.
[37] A. van Le, G. de Saxcé, Exact expression for the plastic corrections and the consistent tangent modulus in rate-independent elastoplasticity, in: European Congress on Computational Methods in Applied Sciences and Engineering, ECCCOMAS, Barcelona, September 11—14, 2000.
[38] J.-P. Ponthot, An extension of the radial return algorithm to account for rate-dependent effects in frictional contact and visco-plasticity, J. Mater. Process. Technol. 80–81 (1998) 628–634.
[39] X.-D. Liu, S. Osher, Convex ENO high order schemes without field-by-field decomposition or staggered grids, J. Comput. Phys. 142 (1998) 304–330.
[40] L. Tran, R. Vilsmeier, D. Haenel, A local level set method for the treatment of discontinuities on unstructured grids, in: Finite Volumes for Complex Application II, Hermes Science Publications, Paris, 1999, pp. 849–856.
[41] R. Menikoff, Errors when shock waves interact due to numerical shock width, SIAM J. Sci. Stat. Comput. 15 (5) (1994) 1227–1242.
[42] R. Donat, A. Marquina, Capturing shock reflections: an improved flux formula, J. Comput. Phys. 125 (1996) 42–58.

[43] R.P. Fedkiw, A. Marquina, B. Merriman, An isobaric fix for the overheating problem in multimaterial compressible flows, J. Comput. Phys. 148 (1999) 545–578.
[44] D.J. Benson, A mixture theory for contact in multi-material Eulerian formulations, Comput. Methods Appl. Mech. Engrg. 140 (1997) 59–86.
[45] C.S. Peskin, Numerical analysis of blood flow in the heart, J. Comput. Phys. 25 (1977) 220–252.
[46] M. Sussman, P. Smereka, S. Osher, A level set approach for computing solutions to incompressible two-phase flow, J. Comput. Phys. 114 (1994) 146–159.
[47] R.J. Leveque, Z. Li, The immersed interface method for elliptic equations with discontinuous coefficients and singular sources, SIAM J. Numer. Anal. 31 (4) (1994) 1019–1044.
[48] D. Adalsteinson, J. Sethian, A fast level set method for propagating interfaces, J. Comput. Phys. 118 (1995) 269–277.
[49] D. Peng, B. Merriman, S. Osher, H.-K. Zhao, M. Kang, A PDE-based fast local level set method, J. Comput. Phys. 155 (1999) 410–438.
[50] Y.Y. Zhu, S. Cescotto, Unified and mixed formulation of the 4-node quadrilateral elements by assumed strain method: application to thermomechanical problems, Int. J. Numer. Methods Engrg. 38 (1995) 685–716.
[51] J.O. Hallquist, DYNA3D User's Manual, University of California, Lawrence Livermore Laboratory, Livermore, 1987.
[52] C.E. Anderson Jr., V. Hohler, J.D. Walker, A.J. Stilp, Time-resolved penetration of long rods into steel targets, Int. J. Impact Engrg. 16 (1) (1995) 1–18.
[53] F.P. Bowden, A.D. Yoffe, Initiation and Growth of Explosions in Liquids and Solids, Cambridge University Press, Cambridge, 1952.
[54] M.M. Carroll, A.C. Holt, Static and dynamic pore-collapse relations for ductile porous materials, J. Appl. Phys. 43 (4) (1972).
[55] J. Kang, P.B. Butler, M.R. Baer, A thermomechanical analysis of hot spot formation in condensed-phase, energetic materials, Combust. Flame 89 (1992) 117–139.
[56] B.A. Khasainov, A.A. Borisov, B.S. Ermolaev, A.I. Korotkov, Two phase visco-plastic model of shock initiation of detonation in high density pressed explosives, in: Seventh Symposium (International) on Detonation, Naval Surface Weapons Center, NSWC MP 82-334, 1981.